

THE EFFECT OF IONIZATION VARIANCE ON NUCLEAR-RECOIL DARK MATTER
SEARCHES

by

MITCHELL DOUGLAS MATHENY

BS, University of Colorado Denver, 2016

A thesis submitted to the
Faculty of the Graduate School of the
University of Colorado in partial fulfilment
of the requirements for the degree of
Master of Integrated Sciences
Integrated Sciences Program

Masters Approval Page

This thesis for the Master of Integrated Science degree by

Mitchell Douglas Matheny

has been approved for the
Integrated Sciences Program

by

Amy Roberts, Chair

Anthony Villano, Advisor

Varis Carey, Advisor

Date: August 3rd, 2019

Matheny, Mitchell Douglas (MINS, Integrated Sciences)

The Effect of Ionization Variance on Nuclear-Recoil Dark Matter Searches

Thesis directed by Assistant Professor Amy Roberts

Abstract

Direct detection dark matter experiments are increasingly interested in the low-mass dark matter parameter space, but zero-background low-mass searches require event separation between the electron and nuclear recoil bands, which requires a proper understanding of detector energy reconstruction.

Previous simulations have shown that we do not entirely understand the ionization efficiency (yield) for electron and nuclear recoils, as the assumption that the distribution for the yield is normally distributed for a true recoil energy is violated. Since the yield distribution may directly affect dark matter low-mass limits, it is crucial we understand how the yield is distributed.

A component to understanding the yield distribution is the variance in the number of electron-hole pairs produced or ionization variance. This effect has been studied relatively infrequently as experiments have been interested in large energy deposits (10 - 100 keV) and could accurately separate electron and nuclear recoil events. For electron recoils, the ionization variance is described by a “Fano” factor. For nuclear recoils the effect can be parameterized by an “effective” Fano factor, which has similar definition but a different physical origin. The nuclear recoil “effective” Fano factor is shown to be much larger than the electron-recoil version above around 10 keV deposited energy.

Approved: Amy Roberts

Contents

| | | |
|-----------|---|-----------|
| I | Dark Matter | 1 |
| 1.1 | Introduction | 1 |
| 1.2 | Velocity Profile and Galactic Rotation Curves | 1 |
| 1.3 | Gravitational Lensing | 3 |
| 1.4 | Dark Matter Candidates | 5 |
| 1.4.1 | Axions | 5 |
| 1.4.2 | Sterile Neutrinos | 6 |
| 1.4.3 | Weakly Interacting Massive Particles | 7 |
| 1.5 | Direct Detection of WIMP Dark Matter | 8 |
| 1.6 | Lindhard Model | 11 |
| 1.7 | Simulated Recoil Bands and Limits | 13 |
| 1.8 | Ionization Variance | 16 |
| II | Simulation: Recoil Band Structure | 21 |
| 2.1 | Charge and Phonon Resolution | 21 |
| 2.1.1 | Recoil Bands from data | 22 |
| 2.2 | Simulated Recoil Bands | 23 |
| 2.2.1 | Electron Recoils: No Fano Factor | 23 |
| 2.2.2 | Containment fraction | 24 |
| 2.2.3 | Nuclear Recoil Band | 28 |
| 2.3 | Fano Factor in Resolutions | 33 |

| | | |
|------------|--|-----------|
| 2.4 | Fano Factor: Varying Number of Electron Hole Pairs | 38 |
| 2.5 | Test of Normality | 43 |
| III | Simulated Yield Distribution Analysis | 49 |
| 3.1 | Two Independent Normal Distributions | 50 |
| 3.1.1 | Model Validation | 51 |
| 3.2 | Two Dependent Normal Distributions | 53 |
| IV | Impact on Dark Matter Searches | 56 |
| 4.1 | $E_Q E_P$ Space | 57 |
| 4.2 | WIMP Mass Accessible | 61 |
| 4.2.1 | Effect on Dark Matter Limit | 63 |
| | Appendices | 64 |
| A | Simulation Algorithm | 65 |
| 1.1 | Simulated Recoil Band Algorithm | 65 |
| 1.2 | Expected Yield Algorithm | 66 |
| B | Distribution Plots | 68 |
| 2.1 | Electron Recoils: Fano = 0.13 | 68 |
| 2.2 | Nuclear Recoils: E_r Dependent Fano Factor | 73 |
| C | Yield Distribution | 78 |

List of Tables

| | | |
|-----|--|----|
| 2.1 | Detector resolution coefficients. α , β , and γ are found from lines of best fit in [29] for detector 1. | 22 |
| 2.2 | Containment fraction for Electron recoil band. The expected 68% containment fraction is under the assumption that the yield for electron recoils is normally distributed. | 27 |
| 2.3 | Containment fraction for Nuclear recoil band simulated with no Fano factor. The expected 68% containment fraction is under the assumption that the yield for nuclear is normally distributed. | 30 |
| 2.4 | Containment fraction for Electron recoil band with a Fano factor of 0.2. The expected 68% containment fraction is under the assumption that the yield for electron recoils is normally distributed. | 40 |
| 2.5 | 1σ Containment fraction for Nuclear recoil band simulation using Edelweiss parameterized Fano factor. The expected 68% containment fraction is under the assumption that the yield for electron recoils is normally distributed. | 40 |
| 2.6 | Results of the distribution analysis for all 8 logarithmically spaced bins from 10 keV 110 keV for the electron recoils. P-value represents significance for both Shapiro-Wilk and Kolmogorov-Smirnov tests for normality. P-Value < 0.01 indicates that the distribution(s) are not normally distributed. | 45 |

| | | |
|-----|---|----|
| 2.7 | Results of the distribution analysis for all 8 logarithmically spaced bins from 10 keV 110 keV for nuclear recoils. P-value represents significance for Shapiro-Wilk test for normality. any P-value < 0.05 indicates rejection of the null hypothesis that the distribution is normal. | 45 |
|-----|---|----|

List of Figures

- 1.1 Rotation curves of spiral galaxies showing the rotational velocity of astrophysical bodies as a function of their distance from the center of the galaxy. Solid line is the expected velocity, dots are from observations [1] 3
- 1.2 Right, Optical images from the Magellan telescope with overplotted contours of spatial distribution of mass, from gravitational lensing . Left, The same contours overplotted over Chandra x-ray data that traces hot plasma in a galaxy. It can be seen that most of the matter resides in a location different from the plasma (which underwent frictional interactions during the merger and slowed down)[2]. 4
- 1.3 Expected WIMP spsctrum for 3 potential masses. X-axis represents energy deposited in the detector with the x-intercept representing the maximum amount of energy transfer possible for the given mass. The shaded region around each line represents the 90% confidence regions. 8
- 1.4 Sketch of a CDMS iZIP detector showing charge and phonon propagation. Here, the liberated charge drifts across the detector due to an applied voltage. The liberated charge excites 'Prompt' phonons (also known as primary phonons) which get collected by phonon sensors. 9
- 1.5 Ionization Yield vs recoil energy from Californium calibration data. Top band represents the electron recoil band, bottom band represents nuclear recoil band. Solid Black bands represent 2.5σ fits to each band. [20] 10

| | | |
|------|--|----|
| 1.6 | Comparison of expected ionization yield to measurements made by several experiments showing a deviation from theory for most experiments. | 12 |
| 1.7 | TOP. Simulated electron and nuclear recoil bands and a function of recoil energy (Pr) found in [22]. Bottom. Electron and nuclear recoil bands from Cf calibration data. Blue and red bands are formed by fitting the ionization yield (y-axis) with a Gaussian and calculating the 2.5σ point from the mean and plotting as a function of recoil energy. | 14 |
| 1.8 | Projected exclusion sensitivity for the SuperCDMS SNOLAB direct detection dark matter experiment. The vertical axis is the spin-independent WIMP-nucleon cross section under standard halo assumptions, and the horizontal axis is the WIMP mass, where WIMP is used to mean any low-mass particle dark matter candidate. The blue dashed curves represent the expected sensitivities for the Si HV and iZIP detectors and the red dashed curves the expected sensitivities of the Ge HV and iZIP detectors [23] | 15 |
| 1.9 | Predicted effective Fano factor for 2 assumptions made by Lindhard. Also shown, measurements made by Dougherty in silicon.[21][26] Figure courtesy of Anthony Villano. | 18 |
| 1.10 | Electron and nuclear recoil bands from data taken during a ^{252}Cf calibration. Red and blue lines represent 1.625σ (90%) containment lines formed using Gaussian fits to the quenching factor [25]. | 19 |
| 2.1 | Simulated electron recoil band with no Fano factor. Red dashed line represents the mean yield $Y_{mean} = 1$. Black bands represent 1σ containment for electron recoil bands from CDMS [32]. | 25 |
| 2.2 | Simulated electron recoil band with logarithmically spaced bins from $10\text{ keV} - 110\text{ keV}$ with no Fano factor. Red dashed line represents the mean yield $Y_{mean} = 1$. Black bands represent 1σ containment for electron recoil bands from CDMS [32]. | 26 |

| | | |
|------|---|----|
| 2.3 | Containment fraction for electron recoil band with no Fano factor. As show, the percent of data within 1σ varies wildly from the expected 68%. | 28 |
| 2.4 | Simulated Nuclear recoil band with Fano factor = 0. Red dashed line represents the mean yield $Y_{mean} = 1$. Black bands represent 1σ containment for electron recoil bands from CDMS [32]. | 30 |
| 2.5 | Simulated Nuclear recoil band with Fano factor = 0 binned into 8 logarithmically spaced bins. Red dashed line represents the mean yield. Black bands represent 1σ containment for nuclear recoil bands from CDMS [32]. | 31 |
| 2.6 | Containment fraction as a functuon of energy for the simulated Nuclear recoil band with Fano factor = 0. Red dashed line represents the mean yield $Y_{mean} = 1$. Black bands represent 1σ containment for electron recoil bands from CDMS [32]. | 32 |
| 2.7 | Nuclear recoil Fano factor vs. Recoil energy. | 34 |
| 2.8 | a: Top: Simulated electron recoil band with Fano factor = 0.13 included in the resolutions. Black bands represent 1σ containment bands derived from fitting data. Red dashed line represent mean of recoil band. Bottom: Containment fraction for simulated electron recoil band with fan factor of 0.13. | 36 |
| 2.9 | a: Simulated nuclear recoil band with Fano factor paramerterized from [25] included in the resolutions. Black bands represent 1σ containment bands derived from fitting data. Red dashed line represent mean of recoil band. b: Containment fraction for simulated nuclear recoil band with fan factor parameterized from [25]. | 37 |
| 2.10 | a: Simulated nuclear recoil band with Fano factor paramerterized from [25] included in the resolutions. Black bands represent 1σ containment bands derived from fitting data. Red dashed line represent mean of recoil band. b: Containment fraction for simulated nuclear recoil band with fan factor parameterized from [25]. | 41 |

2.11 a: Simulated nuclear recoil band with Fano factor parameterized from [25] included in the resolutions. Black bands represent 1σ containment bands derived from fitting data. Red dashed line represent mean of recoil band. b: Containment fraction for simulated nuclear recoil band with fan factor parameterized from [25]. 42

2.12 a) Histogram of the electron recoil band yield for the energy bin centered at 15.74 keV. Overlaid is a Gaussian distribution. As shown, there is evidence for a positive skew, as the distribution has a slight tail on the right side. b) QQ plot. The upward curve in the data indicates a positive skew. To see the histograms and QQ plots for each of the 8 energy bins, please refer to the appendix. 47

2.13 a) Histogram of the nuclear recoil band yield for the energy bin centered at 15.74 keV. Overlaid is a Gaussian distribution. As shown, there is evidence for a positive skew, as the distribution has a slight tail on the right side. b) QQ plot. The upward curve in the data indicates a positive skew. To see the histograms and QQ plots for each of the 8 energy bins, please refer to the appendix. 48

3.1 ab) Containment fraction for electron recoils/ nuclear recoils generated with a fano factor included in the charge and phonon resolutions. Black dotted line represents expected containment fraction predicted by the PDF in equation 3.4. 52

3.2 ab) Containment fraction for electron recoils/ nuclear recoils generated with a fano factor included in the charge and phonon resolutions. Black dotted line represents expected containment fraction predicted by the PDF in equation 3.6. 55

| | | |
|-----|--|----|
| 4.1 | Simulated Charge energy (E_Q) - Phonon energy (E_P) plane for electron and nuclear recoils. Simulated for recoil energies ranging from 0 to 20 keV. . . . | 57 |
| 4.2 | E_Q/E_P plan simulated with a Fano factor of 0. Black band represents electron recoils, blue band nuclear recoil bands. Orange and black points represent location of the 2σ mark for each bin. Data points are for to a line to form lower bound for electron recoils and upper bound for nuclear recoils. The red cross represents the intersection of the 2σ bands. | 59 |
| 4.3 | E_Q/E_P plan simulated with a Fano factor of 100. Black band represents electron recoils, blue band nuclear recoil bands. Red and black points represent location of the 2σ mark for each bin. Data points are for to a line to form lower bound for electron recoils and upper bound for nuclear recoils. The red cross represents the intersection of the 2σ bands | 60 |
| 4.4 | Minimum mass acceptable vs nuclear recoil Fano factor. Mass calculated using recoil energy corresponding to the intersection point in figures such as Figure 4.3. | 62 |
| 4.5 | Projected exclusion sensitivity for the SuperCDMS SNOLAB direct detection dark matter experiment. The vertical axis is the spin-independent WIMP-nucleon cross section under standard halo assumptions, and the horizontal axis is the WIMP mass, where WIMP is used to mean any low-mass particle dark matter candidate. The blue dashed curves represent the expected sensitivities for the Si HV and iZIP detectors and the red dashed curves the expected sensitivities of the Ge HV and iZIP detectors [23] | 63 |
| 2.1 | Histogram (a) and Q-Q plot (b) for electron recoils simulated at bin center 11.7 keV | 68 |
| 2.2 | Histogram (a) and Q-Q plot (b) for electron recoils simulated at bin center 15.7 keV | 69 |

| | | |
|------|---|----|
| 2.3 | Histogram (a) and Q-Q plot (b) for electron recoils simulated at bin center 21.3 keV | 69 |
| 2.4 | Histogram (a) and Q-Q plot (b) for electron recoils simulated at bin center 28.8 keV | 70 |
| 2.5 | Histogram (a) and Q-Q plot (b) for electron recoils simulated at bin center 39.4 keV | 70 |
| 2.6 | Histogram (a) and Q-Q plot (b) for electron recoils simulated at bin center 53.1 keV | 71 |
| 2.7 | Histogram (a) and Q-Q plot (b) for electron recoils simulated at bin center 70.4 keV | 71 |
| 2.8 | Histogram (a) and Q-Q plot (b) for electron recoils simulated at bin center 95.1 keV | 72 |
| 2.9 | Histogram (a) and Q-Q plot (b) for nuclear recoils simulated at bin center 11.7 keV | 73 |
| 2.10 | Histogram (a) and Q-Q plot (b) for nuclear recoils simulated at bin center 15.7 keV | 74 |
| 2.11 | Histogram (a) and Q-Q plot (b) for nuclear recoils simulated at bin center 21.3 keV | 74 |
| 2.12 | Histogram (a) and Q-Q plot (b) for nuclear recoils simulated at vbin center 28.8 keV | 75 |
| 2.13 | Histogram (a) and Q-Q plot (b) for nuclear recoils simulated at bin center 39.4 keV | 75 |
| 2.14 | Histogram (a) and Q-Q plot (b) for nuclear recoils simulated at bin center 53.1 keV | 76 |
| 2.15 | Histogram (a) and Q-Q plot (b) for nuclear recoils simulated at bin center 70.4 keV | 76 |

| | |
|---|----|
| 2.16 Histogram (a) and Q-Q plot (b) for nuclear recoils simulated at bin center 95.1 keV | 77 |
|---|----|

CHAPTER I

DARK MATTER

1.1 Introduction

Dark matter is one of the most mysterious problems cosmologists are faced with today. If we could understand the origins and properties, we could clarify many observations, and strengthen our admittedly limited understanding of the universe. This thesis will focus on understanding how to simulate the electron and nuclear recoil bands accurately. As motivation for content covered later in this document, Chapter I will briefly outline the evidence for dark matter, and describe in detail how energy deposited inside a detector is reconstructed. This chapter will also shed light on previous evidence for simulating the nuclear recoil band incorrectly, and introduce how a rarely explored phenomenon, the "Fano factor", and how it might affect the projected dark matter limits in terms of a minimum detectable dark matter mass.

1.2 Velocity Profile and Galactic Rotation Curves

A galaxy is a gravitationally bound system of stars, gas, dust, and as we now believe, dark matter. By studying the velocities of stars distributed throughout galaxies, the cosmological community now largely agrees that dark matter is an important component [1].

The circular velocity of stars can be measured as a function of distance from the center of the galaxy and using the virial theorem, we can get a good approximation of what this profile should look like. The virial theorem states that for a bound system a star gravitationally bound to a galaxy, the average kinetic energy is:

$$\langle KE \rangle = -\frac{1}{2}\langle V \rangle \quad (1.1)$$

For a spiral galaxy,

$$\langle V \rangle = -\frac{GM_{tot}}{R} \quad (1.2)$$

where M_{tot} is the total mass of the galaxy, M_s is the mass of a particular star, and R is the distance that star is away from the center of the galaxy. Using the standard definition for kinetic energy, the velocity of the star is:

$$v_s^2 = \frac{GM_{tot}}{R} \quad (1.3)$$

Where V is the gravitational potential energy of the star.

The first observational evidence against this formulation for the velocity of stars was found by Fritz Zwicky while observing the coma cluster. He discovered that the virial mass, M_{tot} , and the luminous mass (found by using the number of galaxies and a mass to light ration conversion) differed by a factor of 500, implying that most of the mass was a form of "dark matter" [2].

For rotation curves, from equation 1.3, we expect $V \propto \frac{1}{r}$, but looking at Figure 1.1, we can see that this is not the case. The velocity profile flattens instead of dropping as expected. This flattening of the rotation curve indicates that the mass within a radius R from the center of the galaxy obeys a scaling law :

$$M(R) = \frac{3v_{flat}^2 R}{2G} \quad (1.4)$$

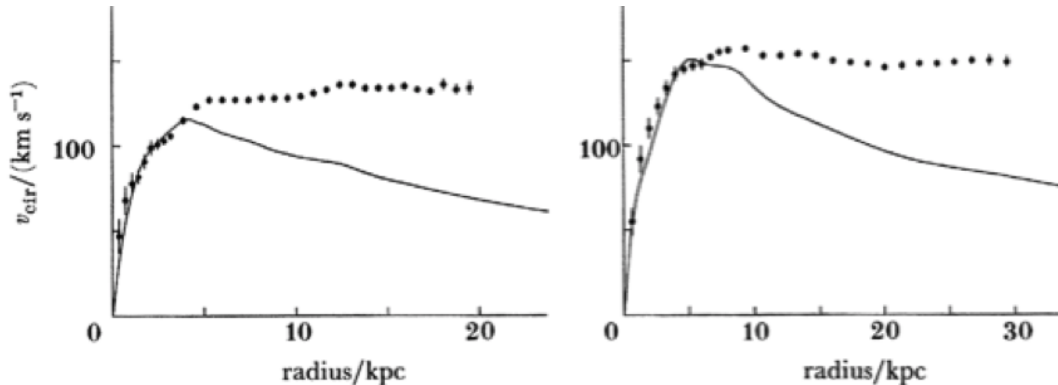


Figure 1.1: Rotation curves of spiral galaxies showing the rotational velocity of astrophysical bodies as a function of their distance from the center of the galaxy. Solid line is the expected velocity, dots are from observations [1]

Assuming the mass is spherically distributed

$$\rho(R) = \frac{3v_{flat}^2}{8\pi GR^2} \quad (1.5)$$

This indicates that the mass seems to increase linearly as a function of distance beyond what can be visibly seen, and has a density that goes as $\frac{1}{R^2}$ far from the edge [3]. This gave rise to the view that a sphere of dark matter resides in a halo surrounding the disk of visible stars and gas in a galaxy.

1.3 Gravitational Lensing

General Relativity predicts that light should deflect, or bend, around a gravitational potential created by a large mass, thus creating a lens. The simplest example of a gravitational lens is a Schwartzchild lens [4]. The angular deflection around a point like mass is

$$\Theta = \frac{4GM}{rc^2} = \frac{2R_s}{r} \quad (1.6)$$

where M is the mass of the lens, R_s is the Schwarzschild radius, and r is the distance from observer and the image of the source [5]. Assuming a simple treatment in which the object of interest is directly behind the lens and the same distance away from that the lense that the observer is, we can find the mass of the lens. Leaving the derivation to [3], the mass is

$$M_{lens} = \frac{c^2 d \tan(\theta_{obs})(\pi - 2\theta_{obs})}{4G} \quad (1.7)$$

Where d is the distance to the lens, c is the speed of light, G is the gravitational constant, and θ_{obs} is the observed angle of deflection. Experiments have observed that the observed angle of deflection is to great for the amount of luminous mass contained in a galaxy, once again indicating the presence of dark matter. It is interesting to note that this simple treatment of a point like mass breaks down when we consider a continuous mass distribution, but this treatment was well suited for one of the more famous confirmations of General Relativity when Arthur Eddington went on an expedition to measure the deflection of light around the sun in 1919 [6].

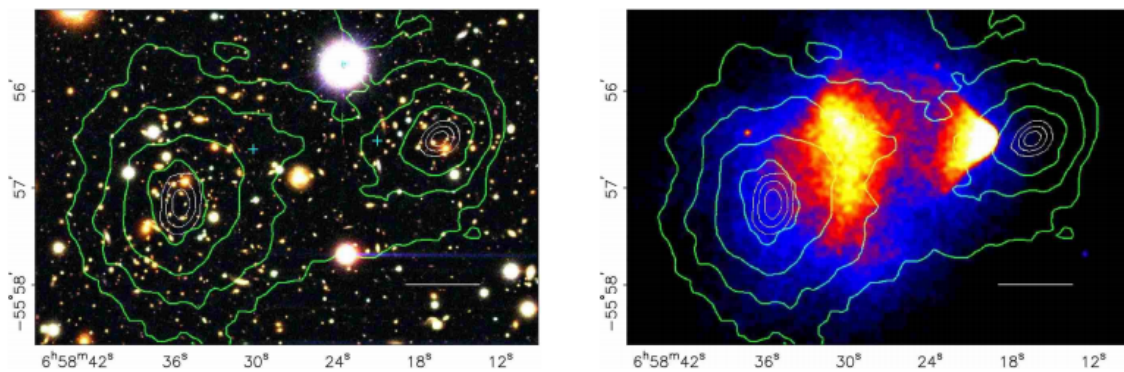


Figure 1.2: Right, Optical images from the Magellan telescope with overplotted contours of spatial distribution of mass, from gravitational lensing . Left, The same contours overplotted over Chandra x-ray data that traces hot plasma in a galaxy. It can be seen that most of the matter resides in a location different from the plasma (which underwent frictional interactions during the merger and slowed down)[2].

An interesting property of dark matter is that it does not interact with itself.

Gravitational lensing presents strong evidence for this observation. A cluster named the "Bullet Cluster" contains the remains of two sub clusters after they collided. Figure 1.2

shows the cluster after the merger in the visible spectrum (left plot) and in xray (right plot). Looking at the left plot, there is no evidence of dark matter (as expected), but looking at right plot, we can see that the amount of lensing, shown as the green contours, is displaced from where the heated gas is. This observation indicates that when the two sub clusters collided, most of the mass (dark matter) passed on by without interacting, reinforcing the notion that dark matter does not interact with itself [2].

1.4 Dark Matter Candidates

The observations mentioned in the previous sections are just a small example of many observations and theories that support the existence of dark matter, all of which rely on gravitational interactions. Though there are several dark matter candidates, whether dark matter interacts via the other fundamental forces is currently pure speculation as no experimental evidence exists to support the claim that it does. Currently, dark matter is thought to be composed of non-baryonic material that has mass and does not interact significantly with radiation or ordinary matter. [5]. Modern dark matter searches are focused on identifying a particle that is the lightest supersymmetric particle (LSP), such as Axions, WIMPS, and sterile neutrinos. In this section, I will give a brief introduction into these candidates.

1.4.1 Axions

Axions, perhaps a less popular candidate for dark matter, is a spinless, electrically neutral, very light particle which was initially introduced as a solution to the strong charge conjugation parity symmetry problem (strong CP problem)[7]. The particle's mass, M_A is dependent upon its decay constant f_a .

$$M_A = 6\mu eV \frac{10^{12} GeV}{f_a} \tag{1.8}$$

Since the energy density of cold axions is

$$\Omega_a h^2 = \left(\frac{f_a}{10^{12} \text{GeV}} \right)^2 \quad (1.9)$$

if the mass is $\mathcal{O}(10\mu\text{eV})$ [8], the axion could be a candidate for cold dark matter as $\Omega_a h^2$ could account for the theorized amount of dark matter in the universe.

The Axion Dark Matter experiment (ADMX) is working to detect axions that have converted to photons in a microwave cavity permeated by a magnetic field [9]. With plans to look into the $10\mu\text{eV}$ range, ADMX results have already excluded low mass axions within the range $1.9\mu\text{eV} < M_A < 3.69\mu\text{eV}$ [10][11].

1.4.2 Sterile Neutrinos

Sterile Neutrinos are hypothetical particles that interact only gravitationally and do not interact via any of the fundamental interactions of the Standard Model. A sterile neutrino \mathcal{N} , is an example of decaying dark matter. Through its mixing with the ordinary neutrinos, \mathcal{N} can decay (via Z boson exchange) into three antineutrinos,

$$\mathcal{N} \rightarrow \tilde{\nu} + \tilde{\nu} + \tilde{\nu} \quad (1.10)$$

and a more constraining decay channel where it decays into a neutrino and a photon.

$$\mathcal{N} \rightarrow \nu + \gamma \quad (1.11)$$

To be dark matter, there should be at least 3 sterile neutrinos to account for neutrino mixing and the lifetime of \mathcal{N} should be greater than the age of the Universe [12]. This constraint on the life time of \mathcal{N} mean that the mass of the particle(s) need to be $M_{DM} \leq 400\text{eV}$. The possible decay channels means that it should be detectable. If the mass of \mathcal{N} is constrained to be $0.4\text{keV} \leq M_{DM} \leq 10\text{keV}$ the energy of the photon should be in x-ray spectrum. Experiments such as XMM-Newton, Chandra, and INTEGRAL are

looking for such decays [12][13][14]. Though \mathcal{N} has not been found, and upper bound on the mass has been made, $M_{DM} \leq 4keV$.

1.4.3 Weakly Interacting Massive Particles

The search for dark matter via direct detection techniques has been motivated by the popularity of Supersymmetric models with a stable lightest Supersymmetric particle as their dark matter candidate. For the last 20 years, the focus of these searches has been on ‘Weakly Interacting Massive Particles’ or WIMPS. WIMPS are expected to be electrically neutral, have a mass somewhere between 10 GeV and 100 TeV and should interact with ordinary matter via the weak nuclear force, giving a small but non negligible coupling to standard model particles [15]. WIMPs are proposed to have decoupled from equilibrium with Standard Model particles once the rate of conversion between WIMPs and other particles became less than the expansion rate of the universe. Previously, neutrinos were originally proposed as a WIMP candidate, but the three known neutrinos do not have enough mass to account for the current estimated dark matter density [16].

The rate at which WIMPS are expected to interact with nuclei in a detector is given by:

$$\frac{dR}{dE_r} = \frac{N_T M_T}{2M_w \mu^2} \left[\sigma^{SI} F_{SI}^2(E_R) + \sigma^{SD} F_{SD}^2(E_R) \right] \tau_{halo} \quad (1.12)$$

where M_w is the mass of the wimp, M_T is the mass of the target nuclei, μ is the reduced mass of the system, N_t is the number of nuclei in the target, and E_R is the energy of the nuclear recoil. $\sigma^{SD}, \sigma^{SI}, F_{SD},$ and F_{SI} are the spin dependent and spin independent cross section and nuclear form factors respectively [17]. τ_{halo} is the halo-model form factor, and depends on the the velocities of the WIMPS in the halo which are usually assumed to take on a standard Maxwellian velocity distribution. Figure 1.3 shows the expected recoil spectra for three WIMP masses.

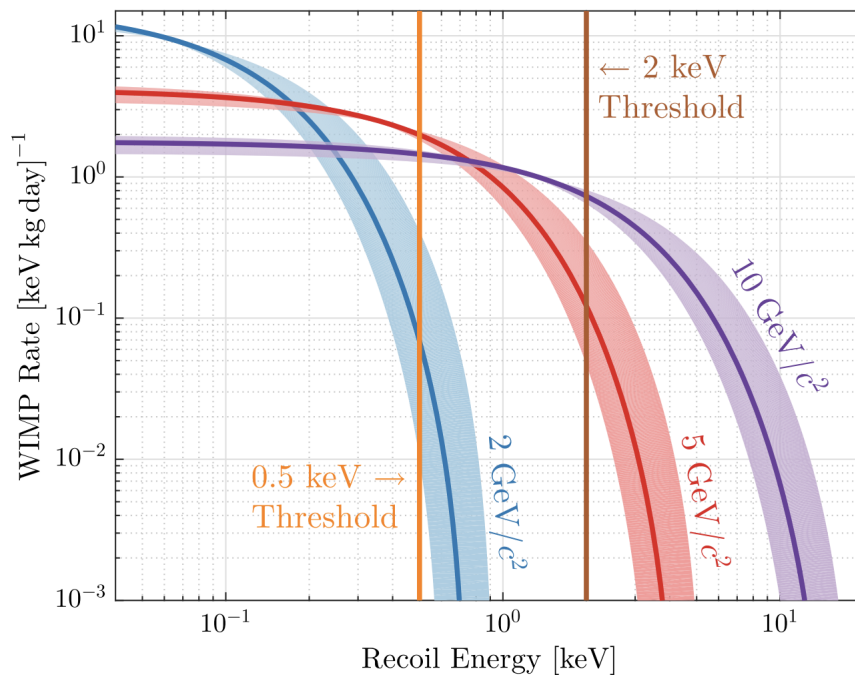


Figure 1.3: Expected WIMP spscrum for 3 potential masses. X-axis represents energy deposited in the detector with the x-intercept representing the maximum amount of energy transfer possible for the given mass. The shaded region around each line represents the 90% confidence regions.

1.5 Direct Detection of WIMP Dark Matter

As mention prior, the primary candidate for direct detection dark matter are WIMPS, and they are expected to interact with the nuclei of the detector. Detecting WIMP dark matter requires a highly sensitive particle detector. The Super CDMS collaboration uses cryogenically cooled Z-sensitive ionization detectors (iZIPS)made of Germanium. These detectors are capable of measuring charge liberated and phonons created through the use of electrodes and superconducting tungsten-aluminum sensors.

When a particle interacts/deposits energy inside a detector, it has two modes of interaction: interacting with the electrons bound the the target's atoms (electron recoils) or scattering off the target nuclei (nuclear recoils). In both cases, it liberates electron holes pairs and produces primary phonons. The electron-hole pairs are drifted across the detector

by a applied volatge. The electron-hole pairs collide with Germanium nuclei and produce secondary or "Luke Phonons [18]." A sketch of this process is visualized in Figure 1.4.

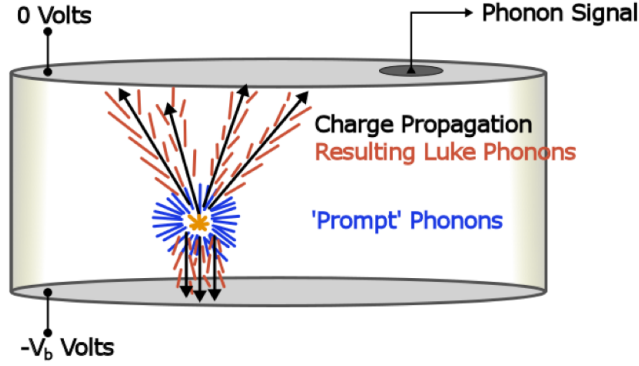


Figure 1.4: Sketch of a CDMS iZIP detector showing charge and phonon propagation. Here, the liberated charge drifts across the detector due to an applied voltage. The liberated charge excites 'Prompt' phonons (also known as primary phonons) which get collected by phonon sensors.

The primary and secondary phonons are detected by aluminum fins that are attached to the transition edge sensors. Any electron hole pairs that are not trapped in a vacancy within the lattice structure drift across the detector until collected by the charge sensors. Determining the energy a particle deposited inside the detector requires measurements of the charge and phonon energy:

$$E_P = E_r + E_{luke} \quad (1.13)$$

$$E_Q = N_{e/h} \epsilon_\gamma$$

where, E_P is the phonon energy, E_{Luke} is the contribution to the total phonon energy from secondary phonons created from drifting electrons [18]:

$$E_{Luke} = eV N_{e/h} \quad (1.14)$$

E_Q is the charge energy, $N_{e/h}$ is the number of electron hole pairs created, and ϵ_γ is the average energy required to liberate 1 electron-hole pair and V is the voltage applied to the

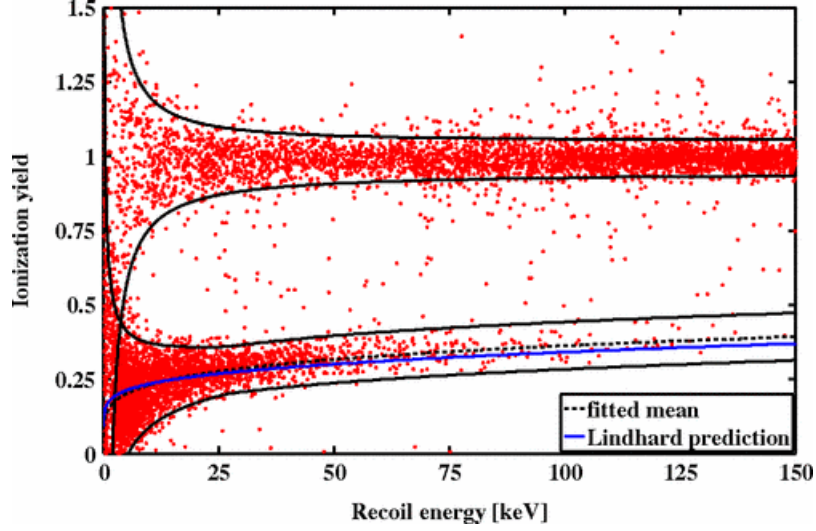


Figure 1.5: Ionization Yield vs recoil energy from Californium calibration data. Top band represents the electron recoil band, bottom band represents nuclear recoil band. Solid Black bands represent 2.5σ fits to each band. [20]

detector. The number of electron-hole pairs created can be expressed in terms of recoil energy:

$$N_{e/h} = \frac{Y E_r}{\epsilon_\gamma} \quad (1.15)$$

where Y is the ionization yield. The ionization yield is the fraction of energy given to the electron-hole pairs. For electron recoils $Y = 1$ and for nuclear recoils the yield is defined by lindhard in [19] and will be discussed in greater detail in the next section. The reconstructed recoil energy is then:

$$E_r = E_P - \frac{V}{\epsilon_\gamma} E_Q \quad (1.16)$$

Figure 1.5 shows the ionization efficiency for both methods of interactions from a CDMS iZIP detector showing the event separation abilities at energies greater than 10 keV.

1.6 Lindhard Model

For CDMS and other charge-based detectors, the question we must answer to reconstruct the energy is: For a nuclear recoil, how much energy is given up to the electronic system? In other words given E_r , what is the ionization yield? In the dark matter community, the most widely used model to answer this question is the Lindhard model. The Lindhard model predicts the fraction of energy given to the electronic system, or ionization yield for nuclear recoils of a given initial kinetic energy. A dislodged nucleus (nuclear recoil) will generally stop in a short distance within a solid. Along the stopping path, the nucleus will interact with either the electronic system or other lattice atoms and generally these energy loss mechanisms compete with one another. The average energy loss due to atomic collisions, $\bar{\nu}(\epsilon)$ is described by the following: [21]

$$k\epsilon^{1/2}\bar{\nu}'(\epsilon) = \int_0^{\epsilon^2} \frac{dt}{2t^{3/2}} f(t^{1/2}) (\bar{\nu}(\epsilon - \frac{t}{\epsilon}) - \bar{\nu}(\epsilon) + \bar{\nu}(\frac{t}{\epsilon})) \quad (1.17)$$

$$\epsilon = E \frac{a}{2Z^2 e^2} \quad (1.18)$$

Where ϵ is dimensionless energy, a is the Bohr radius, Z is the atomic number, e is elementary charge of an electron and t is a variable representing the energy transfer for a scatter of a nuclear recoil with energy ϵ . Solving this equation using a $f(t^{1/2})$ derived from the Thomas-Fermi Potential [21] gives the energy loss due to atomic motion that can be approximated by:

$$\bar{\nu}(\epsilon) = \frac{\epsilon}{1 + kg(\epsilon)} \quad (1.19)$$

$$g(\epsilon) = 3\epsilon^{0.15} + 0.7\epsilon^{0.6} + \epsilon$$

where k is a constant that is determined by the material of interest. For Germanium, the generally accepted value for k is 0.157. As the quantity of interest is the fraction of energy

given to the electrons, or the ionization yield Y , we can use $\bar{\nu}(\epsilon)$ to parameterize this quantity:

$$Y = \frac{\epsilon - \bar{\nu}(\epsilon)}{\epsilon} = \frac{kg(\epsilon)}{1 + kg(\epsilon)} \quad (1.20)$$

A plot of measured values of the ionization yield (ionization efficiency in the plot) for nuclear recoils is shown in Figure 1.6.

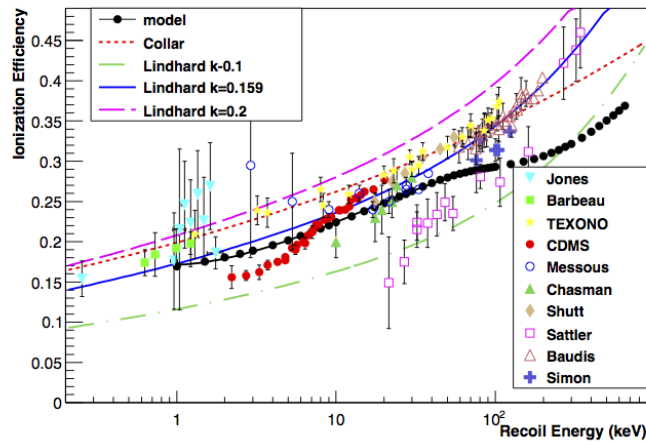


Figure 1.6: Comparison of expected ionization yield to measurements made by several experiments showing a deviation from theory for most experiments.

1.7 Simulated Recoil Bands and Limits

In direct detection dark matter experiments, simulating the electron and nuclear recoil bands is an essential component in understanding detector response. The bands have been previously simulated in [22]. Figure 1.7 shows a comparison of simulated bands to bands created from Cf calibration data. Though not a perfect comparison, one can see that the simulated bands (TOP) are much narrower than the bands from calibration.

Understanding why the bands are narrow is important as it can effect the projected dark matter mass limits. Dark matter mass limits are used to determine what mass, and at what probability, we are expecting to be able to detect dark matter. Figure 1.8 shows current projected CDMS Snow lab limits [23]. The x-axis represent the dark matter, in this case WIMP mass, and the y-axis represents the cross section, or probability of interaction. The narrow simulation bands impacts this plot by shifting where the limits fall. For example, if the simulated bands are really narrow, this could shift a limit down and to the left indicating a stronger limit. This happens because narrow bands indicate that we have the ability to better discriminate between electron and nuclear recoils, meaning that we are more likely to see an interaction for a lower mass dark matter particle, as a low mass particle has a lower maximum possible energy it can deposit. In other words, the better event separation ability, the more confident we are in detecting low mass particle.

The bands simulated in [22] might be too narrow due to not including the ionization variance

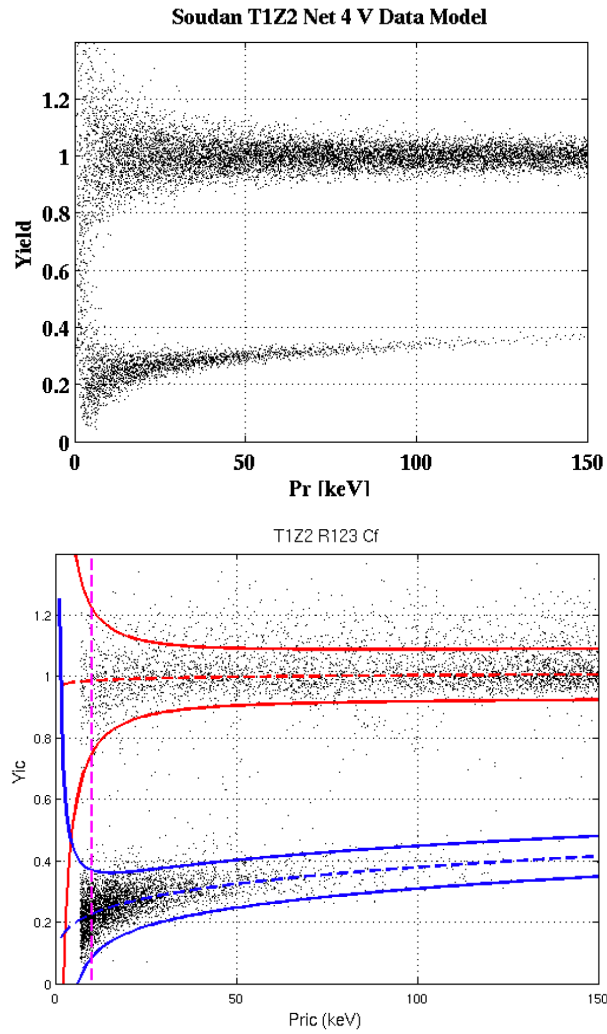


Figure 1.7: TOP. Simulated electron and nuclear recoil bands and a function of recoil energy (Pr) found in [22]. Bottom. Electron and nuclear recoil bands from Cf calibration data. Blue and red bands are formed by fitting the ionization yield (y-axis) with a Gaussian and calculating the 2.5σ point from the mean and plotting as a function of recoil energy.

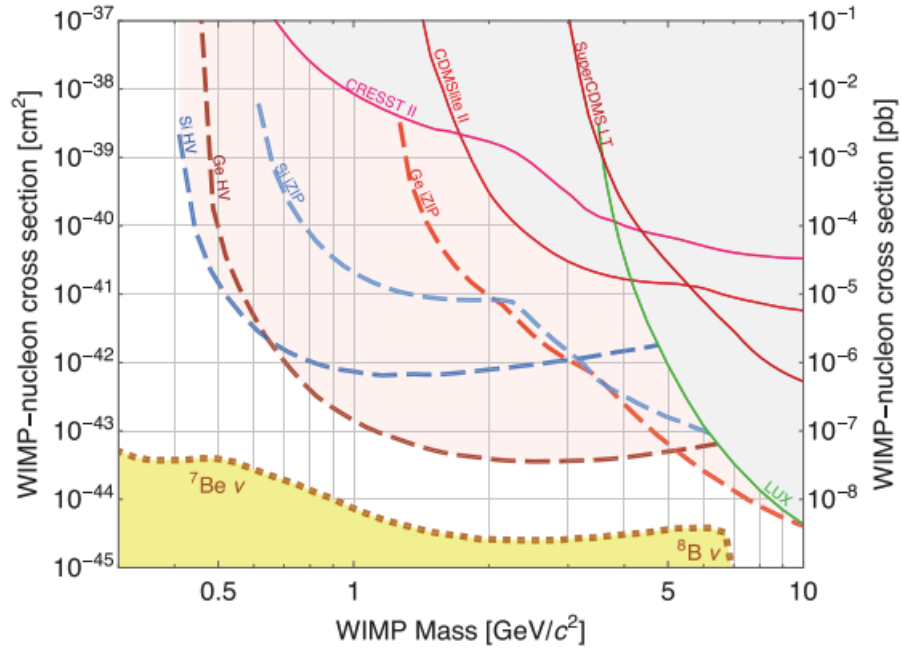


Figure 1.8: Projected exclusion sensitivity for the SuperCDMS SNOLAB direct detection dark matter experiment. The vertical axis is the spin-independent WIMP-nucleon cross section under standard halo assumptions, and the horizontal axis is the WIMP mass, where WIMP is used to mean any low-mass particle dark matter candidate. The blue dashed curves represent the expected sensitivities for the Si HV and iZIP detectors and the red dashed curves the expected sensitivities of the Ge HV and iZIP detectors [23]

1.8 Ionization Variance

The direct detection community has been concerned with the average ionization yield produced by a recoiling nucleus within a detector. This has largely been accepted as experiments such as CDMS, Edelweiss and CRESST were interested in large energy deposits (10-100keV) which allowed the ability to distinguish between electron and nuclear recoils accurately. With the parameter space for WIMP shifting to lower masses, and therfor lower energy deposits, the ability to distinguish between electron and nuclear recoils becomes dependent upon the ionization variance.

In this section, the concept of the Fano factor is introduced for electron recoils followed by an introduction to previous predictions and measurements of the ionization variance and then expressed in terms of an effective nuclear recoil Fano factor. For electron recoils, the variance in the number of electron hole pairs produced for a single recoil is $\sigma_N = \sqrt{FN_{e/h}^-}$, where F is the Fano factor and $N_{e/h}^-$ is the average number of electron hole pairs. The Fano factor is a constant of variation that accounts for the fact that energy loss in particle collision is not purely statistical as an atom has many ways it can ionize. If the variance in electron-hole pair production was purely statistical, the variance would follow that of a Poisson distribution $\sigma_N = \sqrt{N_{e/h}^-}$. For electron recoils in germanium $F = 0.13$ [24]. For nuclear recoils, the concept of the Fano factor is that same for electron recoils as it accounts for the various ways in which a recoiling nucleus can liberate electron-hole pairs. The key difference is that there is evidence that the Fano factor for nuclear recoils is energy dependent. As far as we know, Lindhard, Doughetry, and Edelweiss [25][21][26] are the only ones to make a prediction/measurement for the variation in the number of electron-hole pairs produced. Lindhard predicts a variation in electron-hole pair production Ω^2 , but uses the variation in total energy ϵ so that Ω^2 must also include the variation in phonon energy:

$$\epsilon = \nu(\epsilon) + \eta(\epsilon), \quad (1.21)$$

where ν and η are phonon and ionization energies, respectively. Using this definition, the ionization yield becomes $Y = \frac{\eta}{\epsilon}$. Using the definition of the Fano factor used previously $\sigma_N = \sqrt{FN}$ and the definition of fractional variance $\frac{\sigma_N}{N}$, we can write an effective Fano factor for the nuclear recoil band using Lindhard's notation:

$$\frac{\sqrt{FN}}{N} = \frac{\Omega}{\nu} = \frac{\Omega}{Y\epsilon}$$

$$\frac{NF}{N^2} = \frac{\Omega^2}{Y^2\epsilon^2} \tag{1.22}$$

$$F = \bar{N} \frac{1}{Y^2} \left(\frac{\Omega}{\epsilon} \right)^2$$

This formulation of F only accounting for the variance in electron-hole pair production and not the variation in phonon energy. Figure 4.6 shows effective Fano factors for assumptions (approximations) made by Lindhard in [21] as well as the effective Fano factor measured and predicted by Dougherty for Silicon. As shown, the effective Fano factor is significantly greater than that for electron recoils ($F = 0.13$ for Germanium and $F = 0.115$ for silicon) as there is significant variation in the amount of energy that can be deposited in the phonon system.

Simillaly to CDMS, Edelweiss has the ability to directly measure the ionization yield, expect the use an term called a Quenching factor represented by Q as [25]:

$$Q = \frac{E_I}{E_R} \tag{1.23}$$

$$E_R = \left(1 + \frac{V}{\epsilon}\right)E_H - \frac{V}{\epsilon}E_I$$

Here, E_I is the ionization energy, which is calibrated differently than E_Q , and E_H is the "Heat" Energy which is analogous to E_P . Figure 1.10 shows the measured quenching factor Q vs. E_R for both the electron and nuclear recoil band. Q is parameterized as:

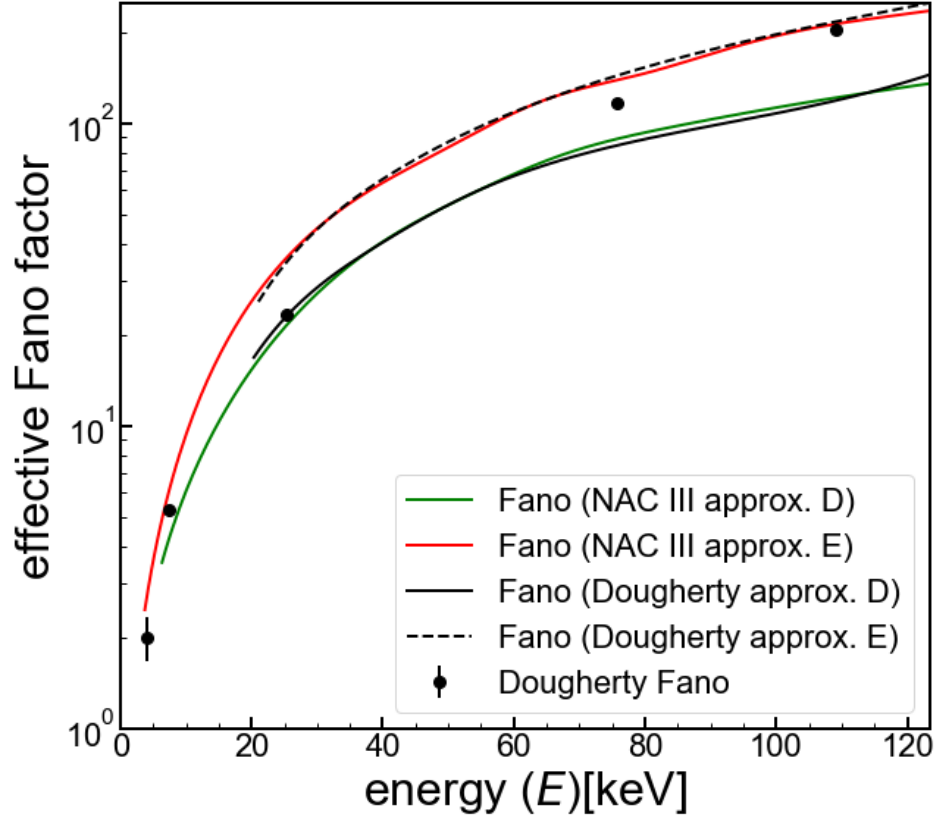


Figure 1.9: Predicted effective Fano factor for 2 assumptions made by Lindhard. Also shown, measurements made by Dougherty in silicon.[21][26] Figure courtesy of Anthony Villano.

where Q is parameterized as:

$$Q = aE_r^b \quad (1.24)$$

where E_r is the recoil energy and $a = 0.16, b = 0.18$.

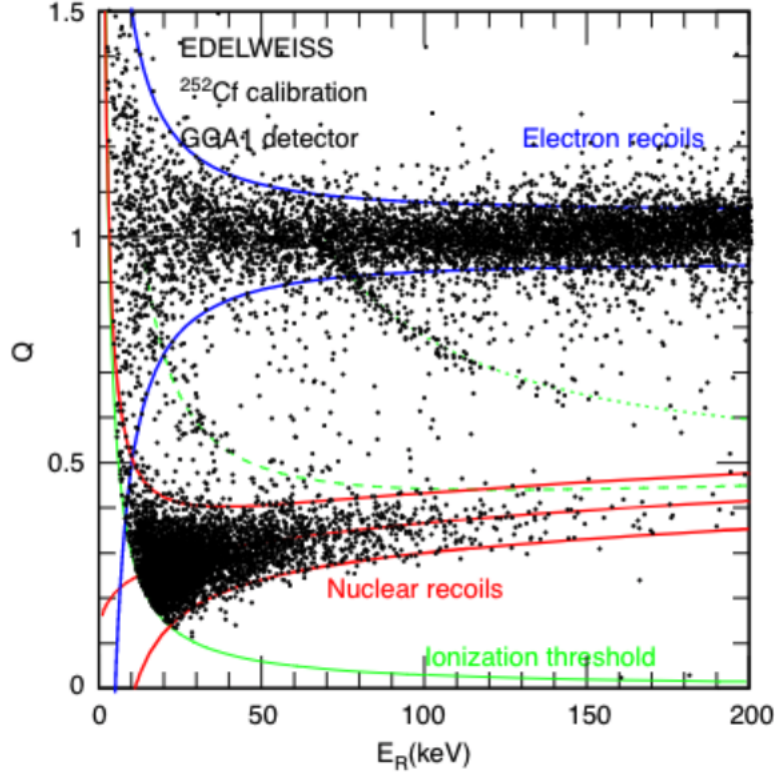


Figure 1.10: Electron and nuclear recoil bands from data taken during a ^{252}Cf calibration. Red and blue lines represent 1.625σ (90%) containment lines formed using Gaussian fits to the quenching factor [25].

Edelweiss made measurements for the variance in the quenching factor:

$$\sigma_Q^2 = \frac{1}{E_R^2} \left(\left(1 + \frac{V}{\epsilon} Q\right)^2 \sigma_I^2 + \left(1 + \frac{V}{\epsilon}\right)^2 Q^2 \sigma_H^2 \right) \quad (1.25)$$

and V is the detector voltage, ϵ is the energy required to create 1 electron hole pair, σ_I^2 is the variance in the charge measurement, σ_H^2 is the variance in the heat measurement [25], σ_I^2 and σ_H^2 are parameterized as:

$$\begin{aligned} \sigma_I(E)^2 &= (\sigma_I^o)^2 + (a_I E)^2 \\ \sigma_H(E)^2 &= (\sigma_H^o)^2 + (a_H E)^2 \end{aligned} \quad (1.26)$$

where σ_I^o and σ_H^o are the baseline resolutions and a_I and a_H are deduced from the resolution of the ionization and heat signals at 122 keV [25].

Edelweiss found that distribution of data was too wide for what they expected. Atomic scattering, variation in the number of charges created by a nuclear recoil [27] and multiple scattering are expected to give an intrinsic width to the Q distribution for nuclear recoils and thus explain this behavior [28]. To account for this, they added a constant in quadrature to the resolution σ_Q^2 :

$$\sigma_{Y(E_R)} = \sqrt{\sigma_Y^o(E_R) + C^2} \quad (1.27)$$

By fitting data, they determined that a typical value of C is 0.04. In the next chapter, the nuclear recoil Fano factor will be parameterized in terms of the Edelweiss resolutions.

CHAPTER II

SIMULATION: RECOIL BAND STRUCTURE

The goal of this thesis is to investigate the role the Fano factor has on setting dark matter mass limits. To do so, we need first to be able to simulate the bands accurately. In the sections that follow, the electron and nuclear recoil bands are simulated in two ways: First, to confirm the narrowness found in the nuclear recoil band by [22], both bands are simulated with no Fano factor. An in-depth analysis of the type of distribution the ionization yield has is also investigated. Second, the bands are simulated by including the Fano factor in the resolutions.

2.1 Charge and Phonon Resolution

An important concept to understand when attempting to simulate the electron and nuclear recoil bands is detector resolution as the value of the resolutions can directly affect the measured ionization yield, which is used to distinguish between the two recoil types and impacts the ability to derive physically accurate detector models. In this section, I give a brief description of how the charge and phonon resolutions for the CDMS iZIP detectors are found and how they will be implemented in simulating the electron and nuclear recoil band.

The charge and phonon resolutions for the iZIP detectors were found by fitting Gaussians to peaks located at 0, 10.36, 66.7, 356, and 511 keV. By comparing the 1σ width of each peak to the associated mean peak location, a functional form was fit for both the phonon and charge resolutions as a function of energy [29]:

$$\begin{aligned}\sigma_p &= \sqrt{\alpha_p + \beta_p E_P + \gamma_p E_P^2} \\ \sigma_q &= \sqrt{\alpha_q + \beta_q E_Q + \gamma_q E_Q^2}\end{aligned}\tag{2.1}$$

where the values for α , β , and γ for σ_p and σ_q are parameters that were computationally found for each CDMS detector. The results for iZIP detector 1 are shown in Table 2.1.

Table 2.1: Detector resolution coefficients. α , β , and γ are found from lines of best fit in [29] for detector 1.

| | α | β | γ |
|------------|----------|------------------|------------------|
| σ_p | 0.155 | $9.1 * 10^{-11}$ | 0.00051 |
| σ_q | 0.166 | 0.0023 | $9.52 * 10^{-5}$ |

2.1.1 Recoil Bands from data

For electron and nuclear recoils, the distribution for the ionization yield is usually modeled to be normally distributed for a given recoil energy. To aid in the analysis of the shape of the electron and nuclear recoils bands, fitted bands from CDMS are used. The black 1σ bands pictured in Figure 2.1 are created by fitting the ionization yield from CDMS data with a Gaussian and calculating the mean and standard deviation. The results from the fit are used to find parameterization of the following form:

$$\mu_Y \pm \sigma_Y\tag{2.2}$$

where:

$$\begin{aligned}\mu_Y &= aE_r^\beta \\ \sigma_Y &= \frac{a^2 E_r^b + c}{E_r}\end{aligned}\tag{2.3}$$

were, a , b , and c are calculated from the fits [30].

2.2 Simulated Recoil Bands

Nuclear recoils are the primary way dark matter is expected to interact with atoms inside a detector. But before trying to simulate the nuclear recoil band, it is essential first to understand how to simulate the electron recoil band, as the electron recoil band has the convenient property that the expected ionization yield is independent of the electron recoil energy, specifically $Y = 1$.

2.2.1 Electron Recoils: No Fano Factor

To simulated the electron recoil band, first a “true” electron recoil energy, E_{er} is randomly drawn from a normal distribution of energies ranging from 10 – 100 keV. This energy is then used to calculate the “tru” phonon energy, charge energy, and average number of electron hole pairs produced $\bar{N}_{e/h}$. The true phonon and charge energies are calculated assuming a perfect resolution:

$$\begin{aligned}\bar{N}_{e/h} &= \frac{E_{er}}{\epsilon} \\ E_P &= E_{er} + V\bar{N}_{e/h} \\ E_Q &= \bar{N}_{e/h}\epsilon\end{aligned}\tag{2.4}$$

here $\bar{N}_{e/h}$ is the average number of electron hole pairs produced, V is the applied detector voltage, and ϵ_γ is the amount of energy needed to liberate 1 electron hole pair. For germanium $\epsilon_\gamma = 3.32 eV$ [31]. To determine a measured yield value, the measured phonon

energy \tilde{E}_P , and the measured charge energy \tilde{E}_Q , it is helpful to have a good understanding of what the distributions for \tilde{E}_P and \tilde{E}_Q are expected to look like. Both \tilde{E}_P and \tilde{E}_Q are expected to be normally distributed:

$$\begin{aligned}
 f(x|\sigma_Q, Y, E_R) &= \frac{1}{\sqrt{2\pi\sigma_Q^2}} e^{-\frac{(x-YE_R)^2}{2\sigma_Q^2}} \\
 f(x|\sigma_P, Y, E_R) &= \frac{1}{\sqrt{2\pi\sigma_P^2}} e^{-\frac{(x-[1+(\frac{eV}{e})Y]E_R)^2}{2\sigma_P^2}}
 \end{aligned}
 \tag{2.5}$$

To simulate these normal distributions the "true" charge and phonon energies are calculated randomly sampling from normal distributions with mean E_p and E_q and standard deviations σ_p and σ_q respectively:

$$\begin{aligned}
 \tilde{E}_P &\approx N(\bar{E}_P, \sigma_p(E_r)) \\
 \tilde{E}_Q &\approx N(\bar{E}_Q, \sigma_Q(E_r))
 \end{aligned}
 \tag{2.6}$$

Using the measured values \tilde{E}_P and \tilde{E}_Q the measured recoil energy and the measured ionization yield can be calculated

$$\begin{aligned}
 \tilde{E}_r &= \tilde{E}_P - \frac{\tilde{E}_Q V}{\epsilon_\gamma} \\
 Y &= \frac{\tilde{E}_Q}{\tilde{E}_r}
 \end{aligned}
 \tag{2.7}$$

Here \tilde{E}_r is the measured electron recoil energy. The result of this simulation is shown below in Figure 2.1

2.2.2 Containment fraction

As mentioned previously, for single recoil energy E_r the yield is expected to be normally distributed and therefore 68.27% of the data should be within 1σ of the mean $Y = 1$. To investigate the amount of data contained within 1σ , the data is generated in logarithmic spaced energy bins from $10keV$ - $110keV$ and the containment fraction is

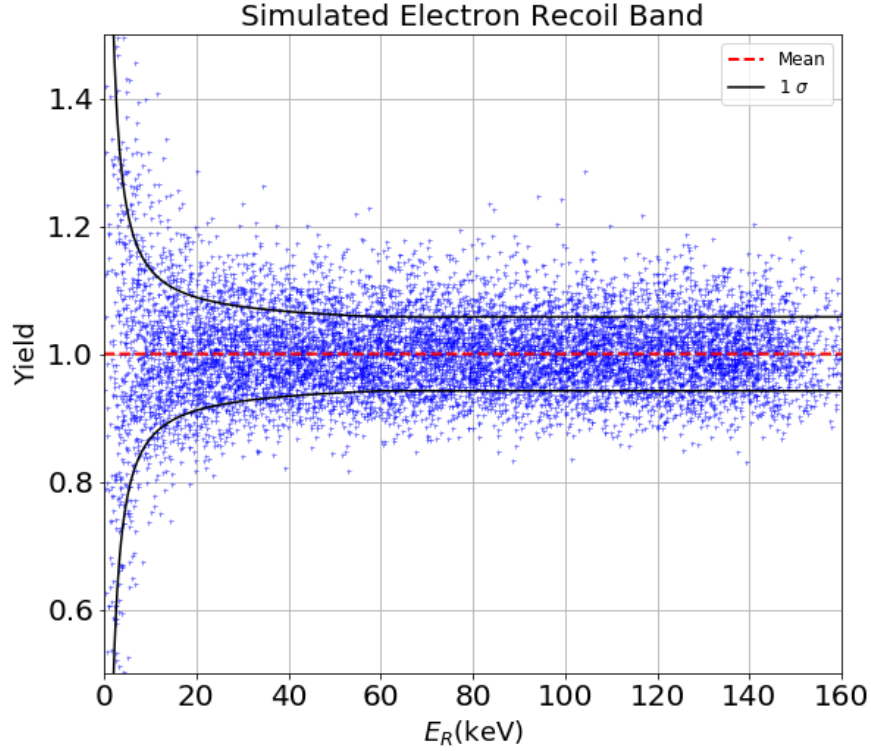


Figure 2.1: Simulated electron recoil band with no Fano factor. Red dashed line represents the mean yield $Y_{mean} = 1$. Black bands represent 1σ containment for electron recoil bands from CDMS [32].

calculated by comparing the amount of data within the 1σ .

$$\%_{contained} = \frac{N - |U + D|}{N} * 100 \quad (2.8)$$

Here, N is the total number of data points in a specific energy bin, U is the amount of data above the upper 1σ band, and D is the amount of data below the lower 1σ band. This counting algorithm follows that of a binomial distribution, allowing for a simple derivation of the uncertainty in the containment fraction:

$$\sigma_c = \frac{\sqrt{Np(1-p)}}{N} \quad (2.9)$$

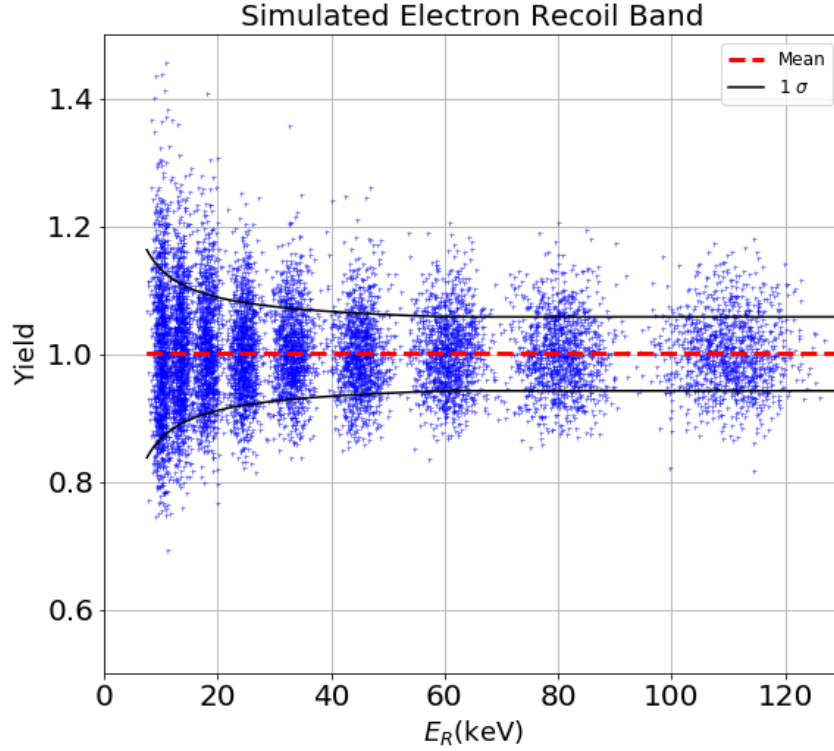


Figure 2.2: Simulated electron recoil band with logarithmically spaced bins from $10 \text{ keV} - 110 \text{ keV}$ with no Fano factor. Red dashed line represents the mean yield $Y_{mean} = 1$. Black bands represent 1σ containment for electron recoil bands from CDMS [32].

where N is the total number of data points within a bin, and p is the probability of success, or number of data points that lay outside the upper and lower 1σ containment bands.

$$p = \frac{N - U - D}{N} \quad (2.10)$$

To quantify the symmetry of the distribution of each bin, the contribution from the upper and lower half of the distribution is calculated:

$$\begin{aligned} \%_{up} &= \frac{N - 2U}{N} * 100 \\ \%_{down} &= \frac{N - 2D}{N} * 100 \end{aligned} \quad (2.11)$$

The containment fraction for each bin is listed in table 2.2 and visualized in Figure 2.3. It

can be seen that the amount of data present within 1σ is greater than 68% for all 8 energy bins. On average, the containment fraction differs from the expected value of 68% by 5.8%. This indicates that the distribution of data in each energy bin is distributed closer to the mean than previously thought, confirming the observation found in [22]. The last two columns in table 2.2 look at the symmetry of the data.

Table 2.2: Containment fraction for Electron recoil band. The expected 68% containment fraction is under the assumption that the yield for electron recoils is normally distributed.

| Energy Bin [KeV] | % Containment | Expected | Percent From High | Percent From Low |
|------------------|------------------|----------|-------------------|------------------|
| 10-13.4 | 81.96 ± 0.41 | 68 | 71.50 ± 0.67 | 78.41 ± 0.59 |
| 13.4-18.1 | 80.23 ± 0.40 | . | 71.91 ± 0.66 | 78.32 ± 0.59 |
| 18.1-24.5 | 78.49 ± 0.42 | . | 71.01 ± 0.67 | 78.30 ± 0.59 |
| 24.5-33.1 | 75.69 ± 0.42 | . | 70.24 ± 0.68 | 76.06 ± 0.62 |
| 33.1-44.8 | 71.88 ± 0.44 | . | 70.24 ± 0.68 | 76.06 ± 0.62 |
| 44.8-60.02 | 69.46 ± 0.43 | . | 65.69 ± 0.71 | 69.22 ± 0.68 |
| 60.6-80.2 | 70.47 ± 0.43 | . | 66.52 ± 0.73 | 70.81 ± 0.55 |
| 80.2-110.0 | 70.13 ± 0.42 | . | 68.39 ± 0.70 | 72.39 ± 0.66 |

Percent from high quantifies the contribution the upper 50% of the data has on the mean of the distribution. Percent from low quantifies the contribution from the lower half of the data. As shown, the contribution from the lower half of the distribution is greater than the upper half, which indicates that the distribution in each energy bin has a positive skew.

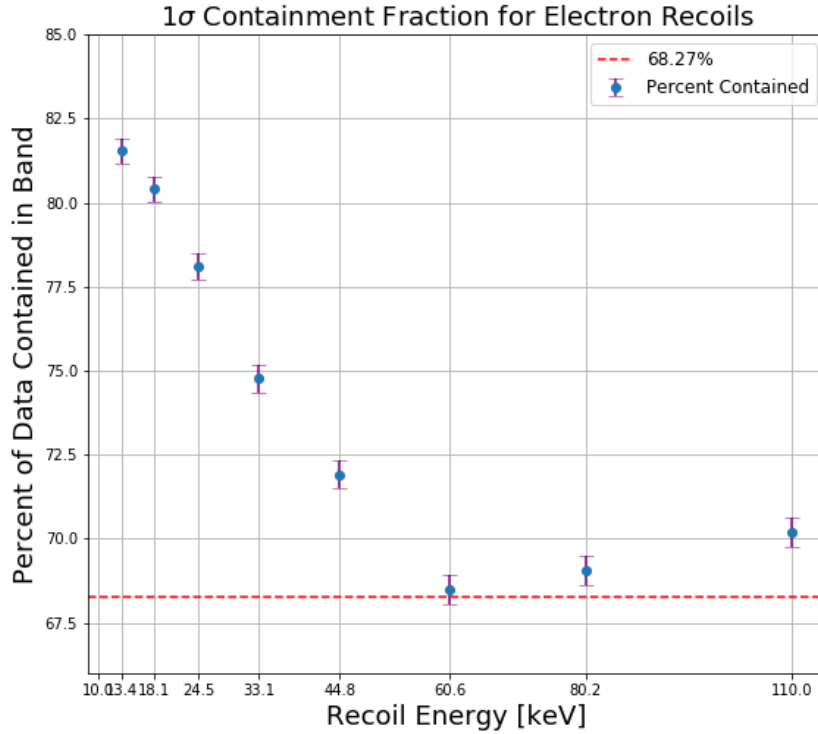


Figure 2.3: Containment fraction for electron recoil band with no Fano factor. As show, the percent of data within 1σ varies wildly from the expected 68%.

2.2.3 Nuclear Recoil Band

As the primary candidate for experiments such as CDMS and Edelweiss are WIMPS, which are expected to interact primarily with the nuclei in a detector, understanding the structure of the nuclear recoil band is important. Simulating the nuclear recoil band is similar to that of the electron recoil band, except the ionization yield is no longer unity and therefore the average number of electron hole pairs created during a nuclear recoil event is now dependent upon the ionization yield Y .

$$N_{e/h}^- = \frac{Y E_{nr}}{\epsilon} \quad (2.12)$$

here Y is defined as the fraction of energy given to the electrons in [19] and originally by Lindhard in [21]:

$$Y = \frac{kg(\epsilon)}{1 + kg(\epsilon)}$$

$$g = 3\epsilon^{0.15} + 0.7\epsilon^{0.6} + 0.6\epsilon \quad (2.13)$$

where k is

$$k = 0.133Z^{\frac{2}{3}}A^{-\frac{1}{2}} \quad (2.14)$$

and ϵ is the reduced energy defined by Lindhard [21] as:

$$\epsilon = E_{nr} \frac{a}{2Ze^2}$$

$$a = 0.8853 \frac{a_o}{2Z^{\frac{1}{3}}} \quad (2.15)$$

where a is a scaled distance, a_o is the bohr radius, Z is the atomic number of both the incoming particle and the target. (Lindhard expresses ϵ in terms of Z_1 and Z_2 , here we look at the case where $Z_1 = Z_2$).

After accounting for the yield, the simulation for the nuclear recoil band is the same as in the previous section (see equations 2.4-2.7). Figure 2.4 shows the results from simulating nuclear recoils with no Fano factor with energies ranging from 0-160 keV. Unlike the electron recoil band, it is visually obvious that the distribution of data is too narrow as almost all of the data falls within the 1σ containment band. To further confirm this observation, that data is split into logarithmically spaced bins as before (shown in figure 4.5) and the percent contained within 1σ is calculated. The results in table 4.4 confirm the visual observation as the average containment fraction is 91.7%. In contrast to the electron recoil band, an interesting observation is that the distribution of the yield appears to be symmetric as the percent from high and percent from low are approximately equal to one

another.

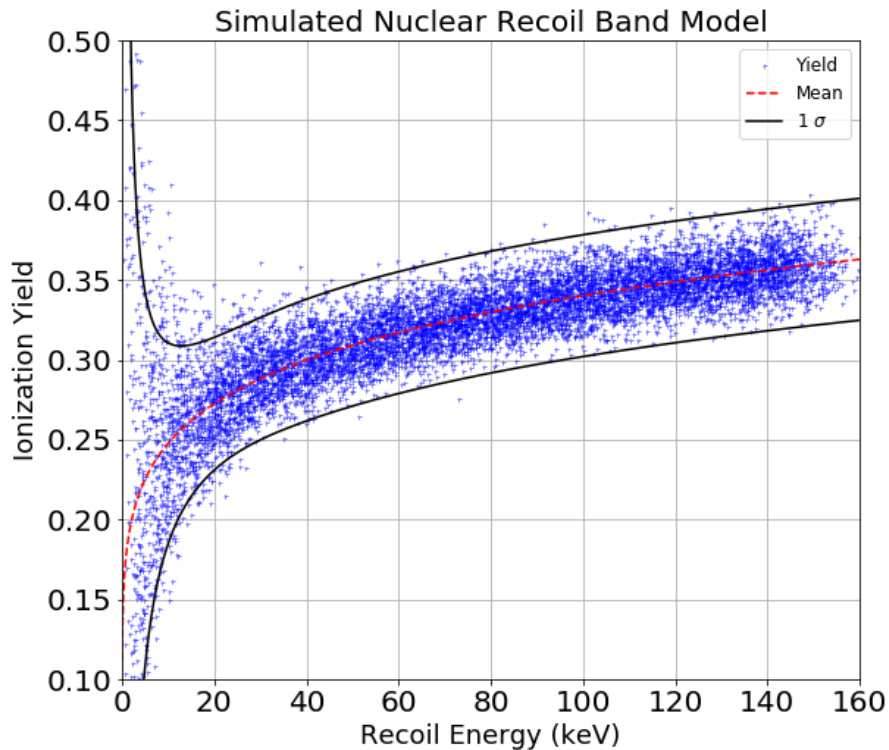


Figure 2.4: Simulated Nuclear recoil band with Fano factor = 0. Red dashed line represents the mean yield $Y_{mean} = 1$. Black bands represent 1σ containment for electron recoil bands from CDMS [32].

Table 2.3: Containment fraction for Nuclear recoil band simulated with no Fano factor. The expected 68% containment fraction is under the assumption that the yield for nuclear is normally distributed.

| Energy Bin [KeV] | % Containment | Expected | Percent From High | Percent From Low |
|------------------|------------------|----------|-------------------|------------------|
| 10-13.4 | 87.09 \pm 1.23 | 68 | 74.33 \pm 2.00 | 79.86 \pm 2.01 |
| 13.4-18.1 | 90.10 \pm 1.61 | . | 76.89 \pm 1.93 | 86.34 \pm 2.24 |
| 18.1-24.5 | 94.80 \pm 1.58 | . | 81.80 \pm 1.80 | 91.47 \pm 2.10 |
| 24.5-33.1 | 96.91 \pm 1.36 | . | 90.84 \pm 1.25 | 97.13 \pm 2.06 |
| 33.1-44.8 | 98.03 \pm 1.23 | . | 95.62 \pm 0.90 | 98.78 \pm 1.84 |
| 44.8-60.02 | 99.40 \pm 1.22 | . | 98.87 \pm 0.42 | 99.83 \pm 1.86 |
| 60.6-80.2 | 99.50 \pm 1.27 | . | 99.45 \pm 0.32 | 99.45 \pm 1.81 |
| 80.2-110.0 | 99.60 \pm 1.15 | . | 99.07 \pm 0.41 | 99.81 \pm 1.55 |

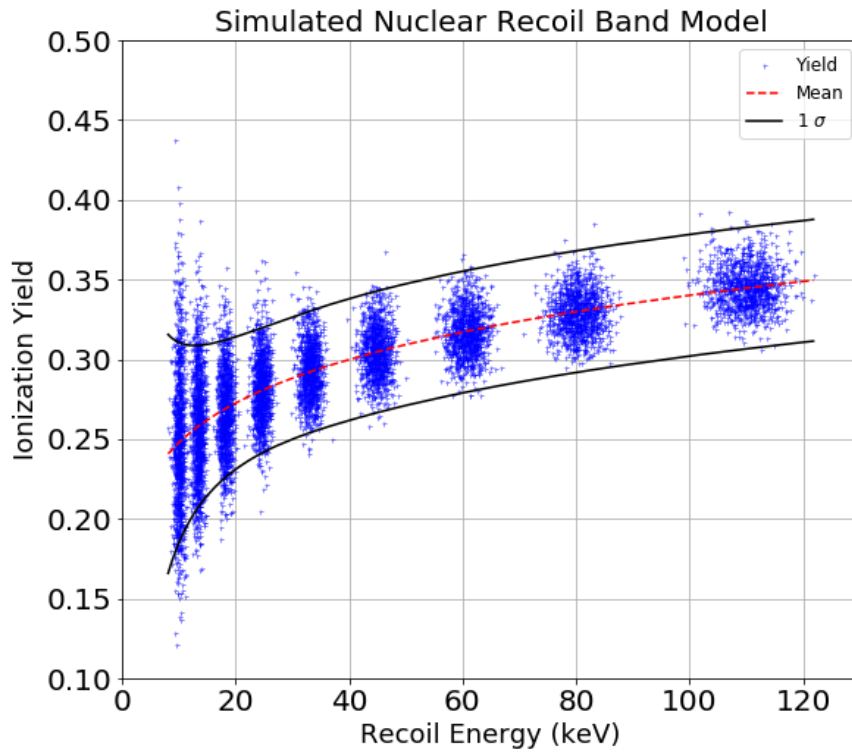


Figure 2.5: Simulated Nuclear recoil band with Fano factor = 0 binned into 8 logarithmically spaced bins. Red dashed line represents the mean yield. Black bands represent 1σ containment for nuclear recoil bands from CDMS [32].

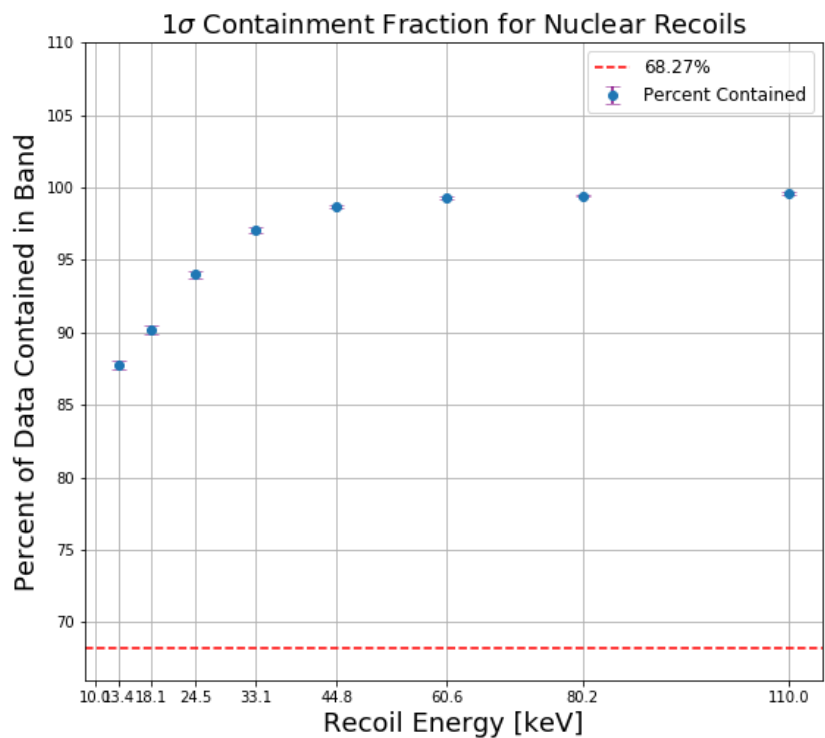


Figure 2.6: Containment fraction as a function of energy for the simulated Nuclear recoil band with Fano factor = 0. Red dashed line represents the mean yield $Y_{mean} = 1$. Black bands represent 1σ containment for electron recoil bands from CDMS [32].

2.3 Fano Factor in Resolutions

As mentioned in Chapter I, the variation in the number of electron hole pairs produced can be expressed as a product of a constant of variation (the Fano factor) and the average number of electron hole pairs produced $N_{e/h}$. While simulating the electron and nuclear recoil bands, we can account for this variation by adding a term to the phonon and charge resolutions:

$$\begin{aligned}\sigma_p &= \sqrt{\alpha_p + \beta_p E_P + \gamma_p E_P^2 + V^2 N_{e/h} F} \\ \sigma_q &= \sqrt{\alpha_q + \beta_q E_Q + \gamma_q E_Q^2 + \epsilon_\gamma^2 N_{e/h} F}\end{aligned}\tag{2.16}$$

what this says is that the charge and phonon measurements should be sensitive to the Fano factor.

Looking at Figure 2.8 and comparing with Figure 2.2, we can see no visual evidence that the width of the yield has been increased for electron recoils. Aside from a variation in the 60.6 keV point in Figure 2.8 bottom, there appeared to be no difference in the containment fraction. This is not all that surprising. With a flat Fano factor of 0.13, the contribution to the resolution is small.

For the nuclear recoil band, the story is a bit different. As mentioned in chapter 1, the form of the Fano factor for the nuclear recoil band is thought not to be constant, but energy dependent. As mentioned, Edelweiss added a constant C to account for the missing variance when comparing their simulation and results from data. If we assume that the extra variance in the variance of the quenching factor σ_Q^2 contributed by C is due to the Fano factor, we can find the Fano factor F as a function of recoil energy and constants a, b, C $F(E_R, C, a, b)$.

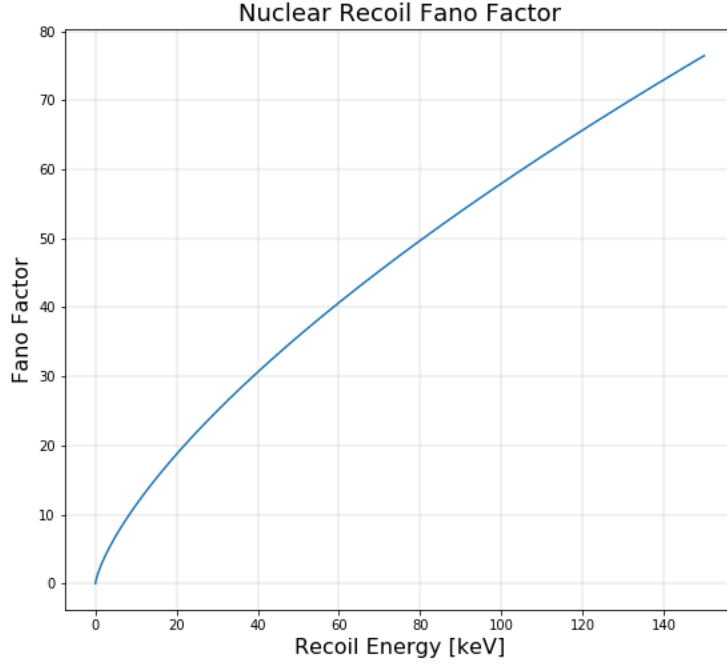


Figure 2.7: Nuclear recoil Fano factor vs. Recoil energy.

$$\sigma_Q^2 = (\sigma_Q^o)^2 + \left(\frac{\epsilon}{E_R} Q + \frac{2V}{E_R} Q^2 + \frac{2V^2}{\epsilon E_R} Q^3 \right) F \quad (2.17)$$

$$F = \frac{C^2}{\left(\frac{\epsilon}{E_R} Q + \frac{2V}{E_R} Q^2 + \frac{2V^2}{\epsilon E_R} Q^3 \right)}$$

where, σ_Q^o is the intrinsic detector resolutions as shown in equation 1.25. Substituting in for Q:

$$F = \frac{C^2}{\left(\frac{\epsilon a}{E_R^{1-b}} + \frac{2V a^2}{E_R^{1-2b}} + \frac{2V^2 a^3}{\epsilon E_R^{1-3b}} \right)} \quad (2.18)$$

Here, a , b and C are constants found from [25]. It is important to note that this formulation of the Fano factor from Edelweiss is an approximation and assumes that the charge and phonon measurements are independent of one another and the yield is normally

distributed, which is actually not the case.

Using this form of the Fano factor in equation 2.16 yields the results shown in Figure 2.9. When comparing the results with Figure 2.5 and 2.6 we can see a significant difference in the width and the containment fraction. The reason for the significant difference, as seen in Figure 2.7, is the fact that the magnitude of the Fano factor increases rapidly with recoil energy and is on average 2 orders of magnitude larger than the electron recoil Fano factor.

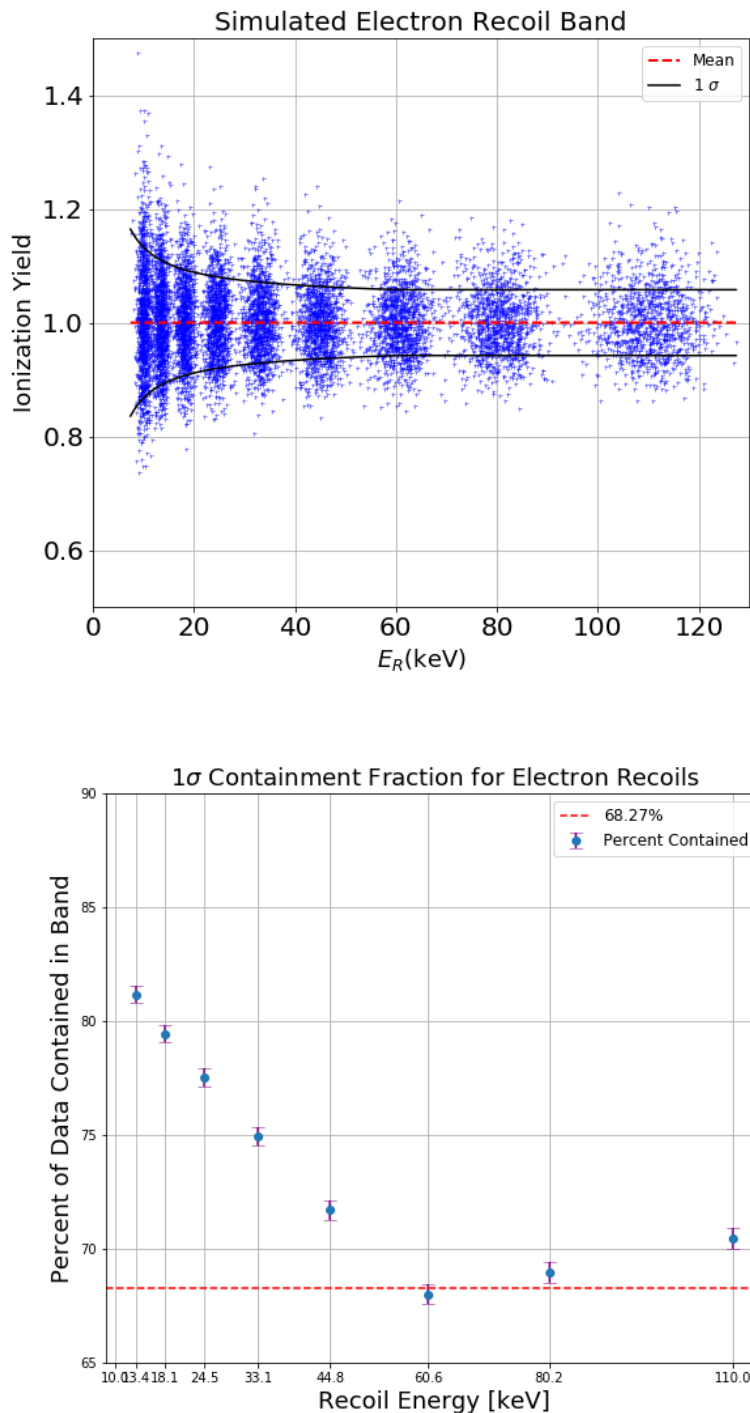
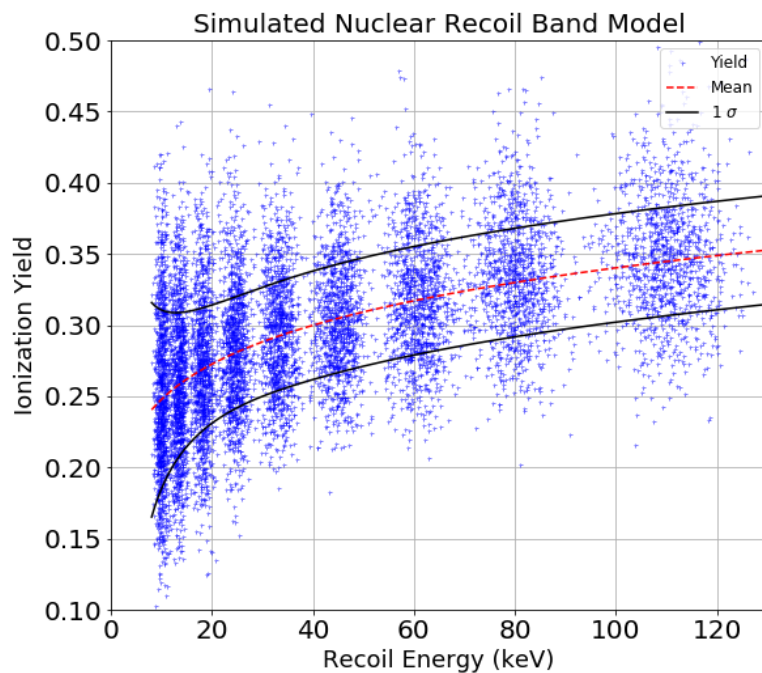
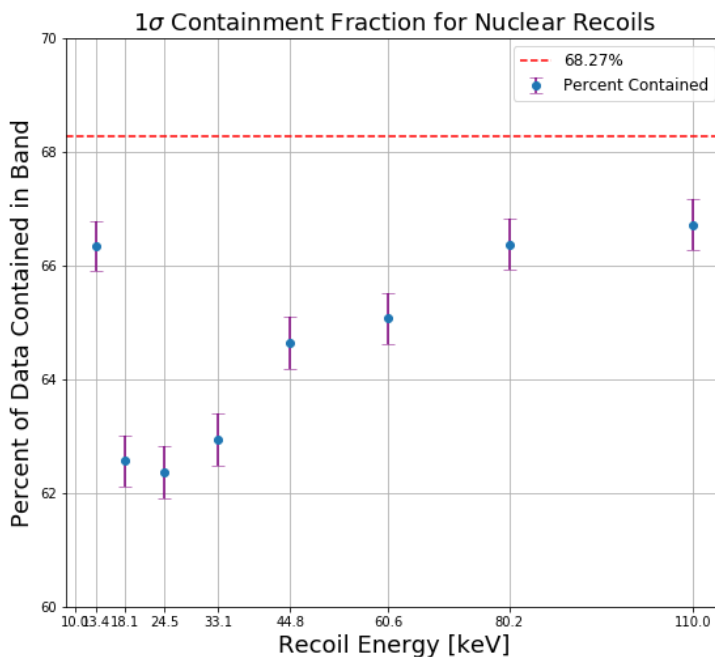


Figure 2.8: a: Top: Simulated electron recoil band with Fano factor = 0.13 included in the resolutions. Black bands represent 1σ containment bands derived from fitting data. Red dashed line represent mean of recoil band. Bottom: Containment fraction for simulated electron recoil band with fan factor of 0.13.



(a)



(b)

Figure 2.9: a: Simulated nuclear recoil band with Fano factor parameterized from [25] included in the resolutions. Black bands represent 1σ containment bands derived from fitting data. Red dashed line represent mean of recoil band. b: Containment fraction for simulated nuclear recoil band with fan factor parameterized from [25].

2.4 Fano Factor: Varying Number of Electron Hole Pairs

In the previous section, the extra variance due to the Fano factor was included in the charge and phonon resolutions. Though it is true that the charge and phonon resolutions are affected by this added variance, including the effective Fano factor in that manner is not entirely a physically accurate model. A more physically accurate model would be to vary the amount of electron hole pairs produced, as an electron or nuclear recoil with a single energy will not produce the same amount of electron hole pairs each time. In other words, an recoil of 60 keV will produce a different amount of electron-hole pairs as a different electron recoil of the same energy. To account for this effect, the mean number of electron hole pairs is varied by randomly sampling from a normal distribution with mean 0 and standard deviation σ_N and adding that number to the mean:

$$\begin{aligned} N_{e/h} &= N(\bar{N}_{e/h}, \sigma_N) \\ \sigma_N &= \sqrt{F \bar{N}_{e/h}} \end{aligned} \tag{2.19}$$

After accounting for the variation in $N_{e/h}$, the “true” values for E_Q and E_P are calculated in the same manner as before:

$$\begin{aligned} E_P &= E_{er} + V N_{e/h} \\ E_Q &= N_{e/h} \epsilon \end{aligned} \tag{2.20}$$

Using the new method of including the Fano factor and following the same method as defined in equations 2.4-2.7, the electron recoil band is simulated. Figure 2.10 and Table 2.4 show the results of the simulation. Comparing the results from the previous section (Figure 2.8), we can see that there is very little difference in amount of data contained in each bin.

For the nuclear recoil band, it is a different story. Figure 2.11 and Table 2.5 shows the results for the nuclear recoil band. Unlike the electron recoil band, there is a significant difference in the containment fraction when comparing to to Figure 2.9. This is due to the

Fano factor increasing as a function of energy. In the first version of including the Fano factor, the contribution was only included in the resolutions, which only effected the range of \tilde{E}_p and \tilde{E}_q values in which we could draw from. By first varying the number of electron holes created, we have a greater fluctuation in the "true" values of E_p and E_q , as there is now 2 sources of fluctuation. ($N_{e/h}$ and sampling from \tilde{E}_p and \tilde{E}_q .) Though also true for the electron recoil band, the contribution from the Fano factor in the nuclear recoil band is 2 orders of magnitude greater and therefore more impactful.

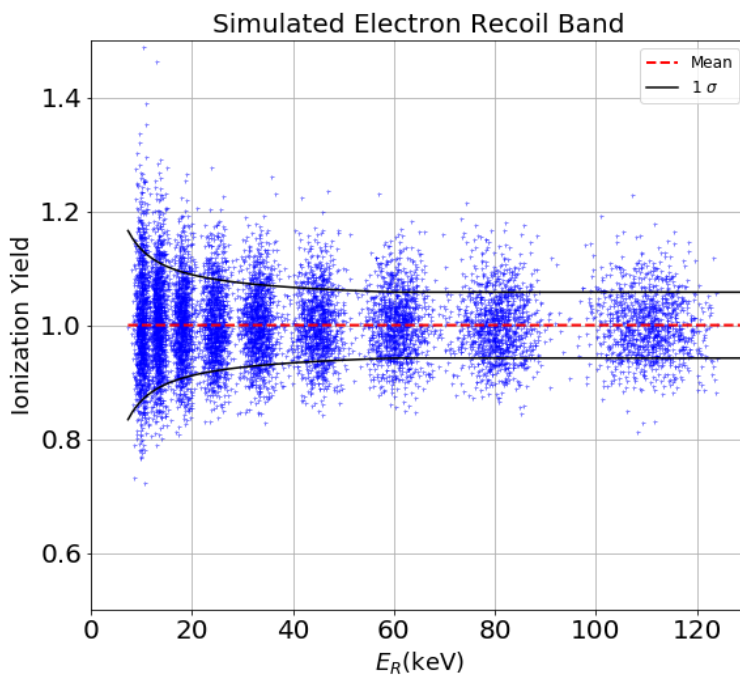
After simulating the electron and nuclear recoil bands with a more physically accurate way of including the Fano factor, it is clear that we do not understand the correct form of the ionization yield distribution. Both CDMS and Edelweiss assume that the yield is normally distributed, however the containment fraction shows that that is not the case. In the next section, the degree in which the distribution for the yield in the electron and nuclear recoil bands deviates from a normal distribution will be investigated.

Table 2.4: Containment fraction for Electron recoil band with a Fano factor of 0.2. The expected 68% containment fraction is under the assumption that the yield for electron recoils is normally distributed.

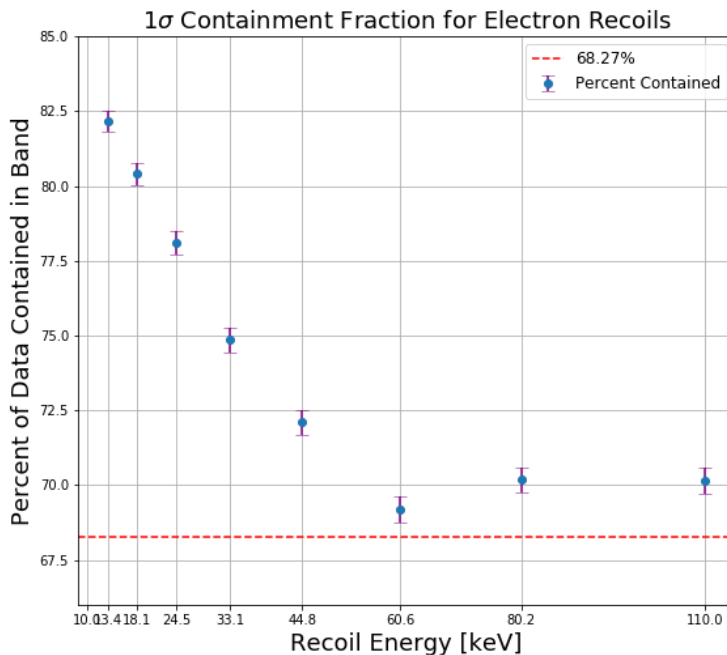
| Energy Bin [KeV] | % Containment | Expected | Percent From High | Percent From Low |
|------------------|------------------|----------|-------------------|------------------|
| 10-13.4 | 81.70 \pm 0.41 | 68 | 71.27 \pm 0.67 | 78.93 \pm 0.58 |
| 13.4-18.1 | 78.83 \pm 0.40 | . | 72.03 \pm 0.66 | 77.86 \pm 0.59 |
| 18.1-24.5 | 78.19 \pm 0.42 | . | 71.59 \pm 0.66 | 77.23 \pm 0.60 |
| 24.5-33.1 | 74.59 \pm 0.43 | . | 70.22 \pm 0.67 | 77.04 \pm 0.60 |
| 33.1-44.8 | 72.18 \pm 0.44 | . | 68.38 \pm 0.69 | 72.64 \pm 0.67 |
| 44.8-60.6 | 67.82 \pm 0.45 | . | 65.47 \pm 0.72 | 70.01 \pm 0.68 |
| 60.6-80.2 | 70.37 \pm 0.43 | . | 65.88 \pm 0.72 | 71.26 \pm 0.67 |
| 80.2-110.0 | 70.60 \pm 0.42 | . | 66.82 \pm 0.70 | 72.88 \pm 0.65 |

Table 2.5: 1σ Containment fraction for Nuclear recoil band simulation using Edelweiss parameterized Fano factor. The expected 68% containment fraction is under the assumption that the yield for electron recoils is normally distributed.

| Energy Bin [KeV] | % Containment | Expected | Percent From High | Percent From Low |
|------------------|------------------|----------|-------------------|------------------|
| 10-13.4 | 74.21 \pm 1.33 | 68 | 61.78 \pm 2.23 | 73.30 \pm 2.01 |
| 13.4-18.1 | 72.59 \pm 1.41 | . | 67.32 \pm 2.21 | 66.25 \pm 2.24 |
| 18.1-24.5 | 72.73 \pm 1.38 | . | 66.79 \pm 2.22 | 70.87 \pm 2.10 |
| 24.5-33.1 | 75.87 \pm 1.36 | . | 69.35 \pm 2.16 | 72.58 \pm 2.06 |
| 33.1-44.8 | 78.16 \pm 1.23 | . | 78.12 \pm 1.88 | 79.20 \pm 1.84 |
| 44.8-60.02 | 79.70 \pm 1.22 | . | 81.96 \pm 1.77 | 80.04 \pm 1.86 |
| 60.6-80.2 | 80.67 \pm 1.23 | . | 76.54 \pm 1.91 | 79.19 \pm 1.81 |
| 80.2-110.0 | 81.60 \pm 1.15 | . | 81.32 \pm 1.76 | 83.88 \pm 1.65 |

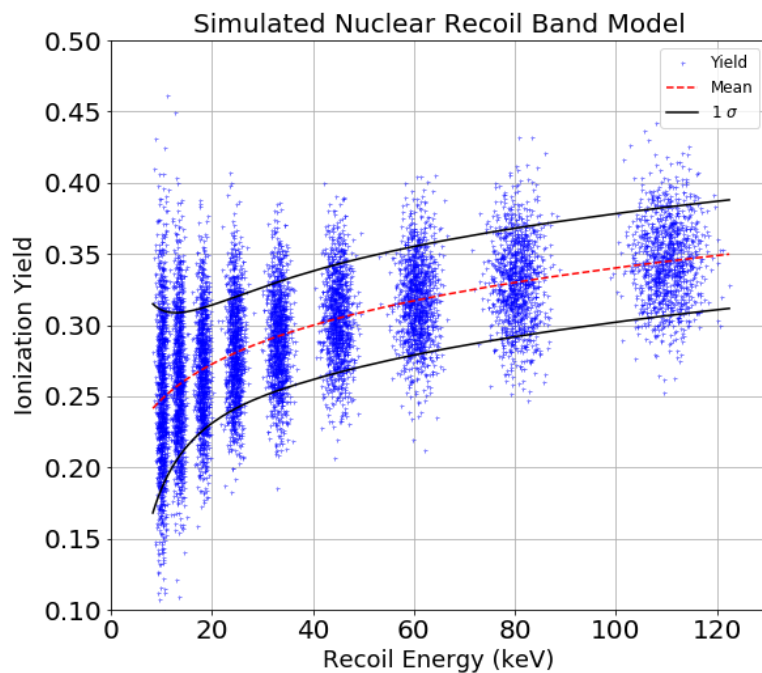


(a)

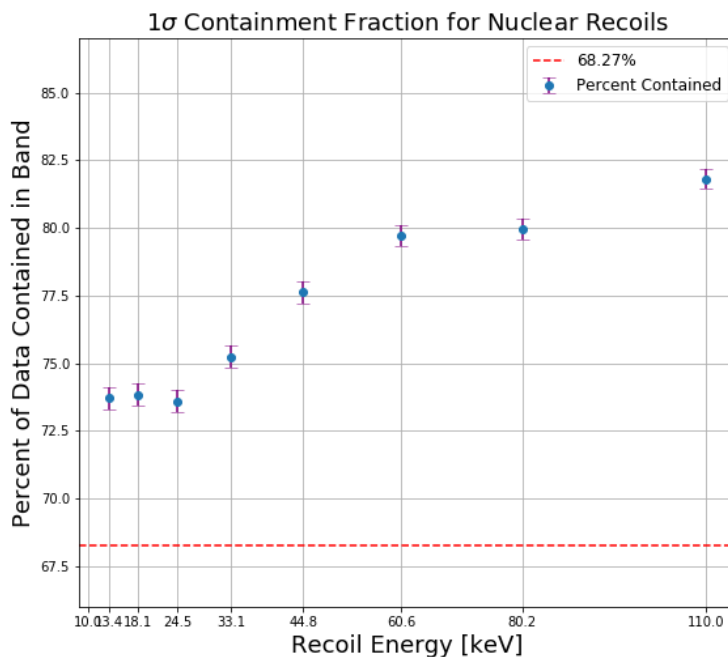


(b)

Figure 2.10: a: Simulated nuclear recoil band with Fano factor parameterized from [25] included in the resolutions. Black bands represent 1σ containment bands derived from fitting data. Red dashed line represent mean of recoil band. b: Containment fraction for simulated nuclear recoil band with fan factor parameterized from [25].



(a)



(b)

Figure 2.11: a: Simulated nuclear recoil band with Fano factor parameterized from [25] included in the resolutions. Black bands represent 1σ containment bands derived from fitting data. Red dashed line represent mean of recoil band. b: Containment fraction for simulated nuclear recoil band with fan factor parameterized from [25].

2.5 Test of Normality

In the previous section, the containment fraction shows that the distributions for the various energy bins for the electron and nuclear recoil band do not contain the amount of data expected from a normal distribution. The containment fraction does not however, grant a sense to what degree these distributions differ from that of a normal distribution. In this section, this deviation will be explored.

Figure 2.12 and Figure 2.13 shows a histogram and a Q-Q plot of the lowest energy bin (bin center at 15.75 keV) for the electron and nuclear recoil band respectively. As shown, there is visual evidence for a asymmetry in both the histogram and the Q-Q plots.

To quantify the amount of asymmetry we can use the skew, also known as the 3rd central moment of a normal distribution, using Pearson's Skewness coefficient G_i [33]. Pearson's coefficient compares the sample to that of a symmetric normal distribution. If the coefficient $G_i = 0$, there is no skew to the distribution and if G_i deviates from zero, it indicates that the distribution has skew. The amount and direction of skew is indicated by the magnitude and sign of G_i . Larger the magnitude, larger the skew, a negative coefficient indicates negative skew, positive coefficient - positive skew. Equation 2.16 describes how the skewness is calculated. To summarize, the traditional way to represent Pearson's skewness coefficient is use the ratio of the 2nd and 3rd moments about the mean i.e $m_2 = \frac{1}{n} \sum_{n=1}^n (x - \bar{x})^2$ and $m_3 = \frac{1}{n} \sum_{n=1}^n (x - \bar{x})^3$.

$$G_i = \frac{m_3}{m_2^{\frac{3}{2}}} = \frac{\frac{1}{n} \sum_{n=1}^n (x - \bar{x})^3}{\left[\frac{1}{n} \sum_{n=1}^n (x - \bar{x})^2\right]^{\frac{3}{2}}} \quad (2.21)$$

The 2nd moment of a normal distribution is also known as the variance. Programs and packages such as Excel and numpy in python use a version that is adjusted for the sample size of the distribution:

$$G_i = \frac{n}{(n-1)(n-2)} \frac{1}{n} \sum_{n=1}^n \left(\frac{x - \bar{x}}{\sigma} \right)^3 \quad (2.22)$$

Using numpy, the skewness in each bin is calculated, the results of which are shown in tables 2.6 and 2.7. As we can see, the Pearson's Skewness Coefficient confirms the observations from Figure 2.12 and 2.13 that the distributions for the yield are positively skewed. To further quantify the distribution of the yield for electron and nuclear recoils, it is important to look at the Kurtosis. Kurtosis, also known as the central 4th moment of a distribution, is a quantitative way to look at the "tailedness" of the distribution.

$$K = \frac{1}{n} \sum_{n=1}^n \left(\frac{x - \bar{x}}{\sigma} \right)^4 \quad (2.23)$$

Values for K range from $1 - \infty$. The larger the value for K , the less normal, or heavy tailed, the distribution becomes. For example, a normal distribution has a value of $K = 3$ and a Cauchy distribution has a value of $K = 66.9$ [34]. The results for K shown in tables 2.6 and 2.7 indicated that the "tailedness" does not deviate from that of a normal distribution with an average percent difference of 9%. To complete the analysis of the normality of the yield, one should test specifically if the data is from a normal distribution. This can be done using a Shapiro-Wilk and Kolmogorov-Smirnov test for normality. The Shapiro-Wilk test for normality calculates a W statistic and tests whether the sample comes from (specifically) a normal distribution.

$$W = \frac{(\sum_{i=1}^n a_i x_i)^2}{\sum_{i=1}^n (x - \bar{x})^2} \quad (2.24)$$

The Kolmogorov-Smirnov test is a non-parametric alternative to the Shapiro-Wilk test as it only assumes that the data is continuous. Shapiro-Wilk assumes that the data is randomly sampled, continuous, and has homoscedasticity (constant variance). It is important to note that both Shapiro-Wilk and Kolmogorov-Smirnov are sensitive to large sample sizes. For a sample size greater than $N = 2000$, both tests have a tendency to increase

the type-1 error. In other words, both tests are extremely sensitive to small deviations from a normal distribution. Therefore, both tests have a significant chance at rejecting the null hypothesis (that the distribution is normal) even when it is true. The sensitivity of both tests means one must use both the tests and the visual representations of the data (histogram and QQ plot) to truly determine whether or not the distributions are normal.

Table 2.6: Results of the distribution analysis for all 8 logarithmically spaced bins from 10 keV 110 keV for the electron recoils. P-value represents significance for both Shapiro-Wilk and Kolmogorov-Smirnov tests for normality. P-Value < 0.01 indicates that the distribution(s) are not normally distributed.

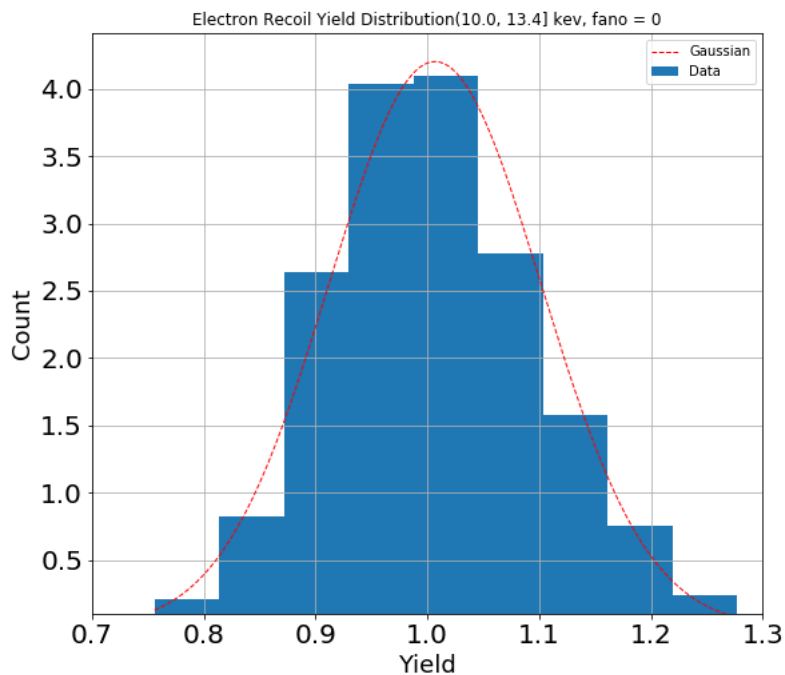
| Energy bin [keV] | G_i | K | Shapiro-Wilk | P-Value _{SW} | Kolm-Smirnov | P-Value _{KS} |
|------------------|-------|-----|--------------|-----------------------|--------------|-----------------------|
| 10-13.4 | 0.41 | 3.5 | 0.92 | < 0.01 | 0.031 | < 0.01 |
| 13.4-18.1 | 0.39 | 3.2 | 0.98 | < 0.01 | 0.028 | < 0.01 |
| 18.1-24.5 | 0.34 | 3.3 | 0.99 | < 0.01 | 0.032 | < 0.01 |
| 24.5-33.1 | 0.33 | 3.7 | 0.98 | < 0.01 | 0.029 | < 0.01 |
| 33.1-44.8 | 0.38 | 3.0 | 0.99 | < 0.01 | 0.031 | < 0.01 |
| 44.8-60.6 | 0.31 | 2.9 | 0.97 | < 0.01 | 0.031 | < 0.01 |
| 30.6-80.2 | 0.29 | 2.9 | 0.96 | < 0.01 | 0.028 | < 0.01 |
| 80.2-110.0 | 0.29 | 2.8 | 0.95 | < 0.01 | 0.032 | < 0.01 |

Table 2.7: Results of the distribution analysis for all 8 logarithmically spaced bins from 10 keV 110 keV for nuclear recoils. P-value represents significance for Shapiro-Wilk test for normality. any P-value < 0.05 indicates rejection of the null hypothesis that the distribution is normal.

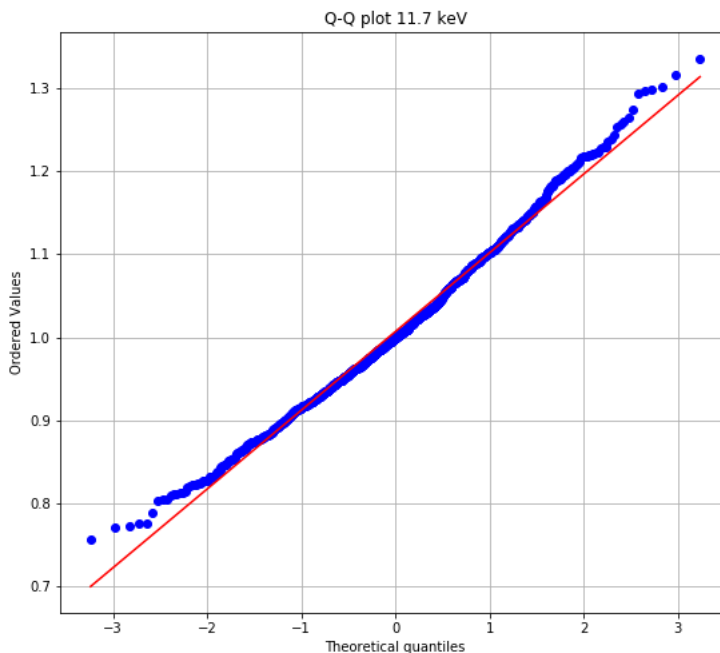
| Energy bin [keV] | G_i | K | Shapiro-Wilk | P-Value _{SW} | Kolm-Smirnov | P-Value _{KS} |
|------------------|-------|------|--------------|-----------------------|--------------|-----------------------|
| 10-13.4 | 0.27 | 3.02 | 0.99 | < 0.01 | 0.022 | < 0.01 |
| 13.4-18.1 | 0.19 | 2.97 | 0.99 | < 0.01 | 0.028 | 0.034 |
| 18.1-24.5 | 0.18 | 3.25 | 0.99 | < 0.01 | 0.032 | 0.02 |
| 24.5-33.1 | 0.09 | 2.82 | 0.98 | < 0.01 | 0.031 | 0.26 |
| 33.1-44.8 | 0.38 | 2.71 | 0.99 | < 0.01 | 0.038 | 0.27 |
| 44.8-60.6 | 0.31 | 2.84 | 0.98 | < 0.01 | 0.032 | 0.45 |
| 30.6-80.2 | 0.29 | 3.07 | 0.99 | < 0.01 | 0.031 | 0.26 |
| 80.2-110.0 | 0.29 | 3.02 | 0.97 | < 0.01 | 0.029 | 0.19 |

The results of the analysis are clear: The ionization yield for the electron and nuclear recoil bands is not normally distributed. There is too much data within 1σ and the distributions are positively skewed. The reason that the data is not normally distributed is due to the functional form of the ionization yield. Equation 2.7 is a ratio of 2 normally

distributed random variables. As it turns out, the distribution of the ratio of two normal distributions is not a normal distribution, but a ratio distribution. The type of ratio distribution depends on whether or not the numerator and denominator are independent or dependent, both of which will be investigated in chapter 3

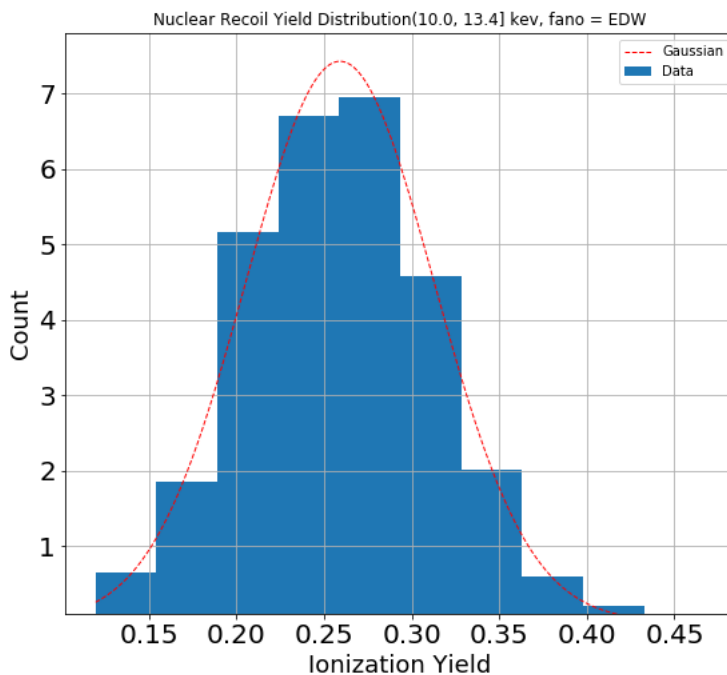


(a)

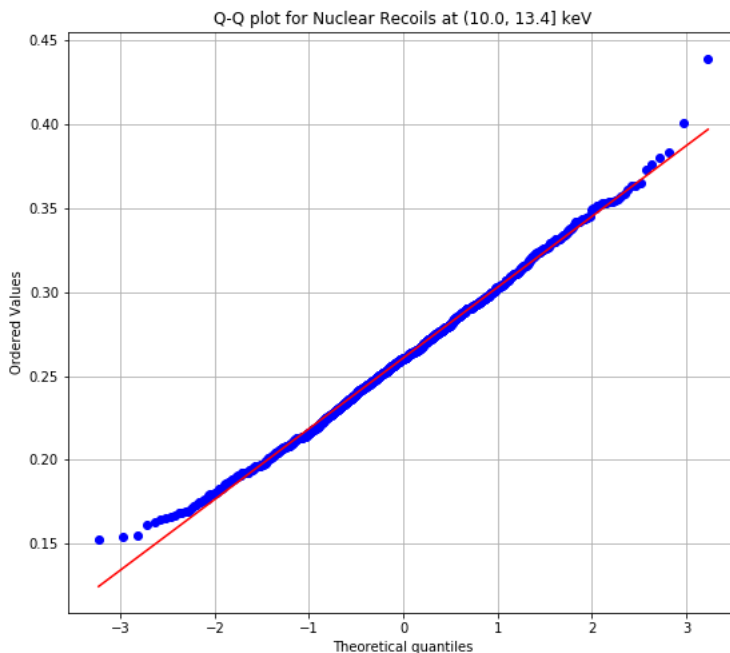


(b)

Figure 2.12: a) Histogram of the electron recoil band yield for the energy bin centered at 15.74 keV. Overlaid is a Gaussian distribution. As shown, there is evidence for a positive skew, as the distribution has a slight tail on the right side. b) QQ plot. The upward curve in the data indicates a positive skew. To see the histograms and QQ plots for each of the 8 energy bins, please refer to the appendix.



(a)



(b)

Figure 2.13: a) Histogram of the nuclear recoil band yield for the energy bin centered at 15.74 keV. Overlaid is a Gaussian distribution. As shown, there is evidence for a positive skew, as the distribution has a slight tail on the right side. b) QQ plot. The upward curve in the data indicates a positive skew. To see the histograms and QQ plots for each of the 8 energy bins, please refer to the appendix.

CHAPTER III

SIMULATED YIELD DISTRIBUTION ANALYSIS

For dark matter searches, confidently knowing the shape in which the probability distribution for the ionization yield takes directly impacts what data in the electron and nuclear recoil band can be accepted or rejected. As mentioned prior, the shape in which the pdf takes has always been assumed to be normal and as shown from the analysis in the previous chapter, this is not the case. The containment fraction for the electron and nuclear recoil band differed significantly from that of a normal distribution for all energies.

In this chapter, an analytical form for the probability distribution of the ionization yield is derived for the two ways in which the data is simulated in chapter II. The first is assuming that the charge energy E_Q and the phonon energy E_P are independent of one another. The second E_Q and E_P are assumed to be dependent.

3.1 Two Independent Normal Distributions

In chapter 2, the yield is simulated by including the fano factor in the charge and phonon resolutions. This way of simulation lets us treat the charge and phonon energy's as if they are independent, or not correlated.

$$Y = \frac{E_Q}{E_p - \frac{V}{\epsilon} E_Q} \quad (3.1)$$

Here E_P and E_Q are normally distributed:

$$\begin{aligned} E_p &\approx N(\mu_p, \sigma_p^2) \\ E_Q &\approx N(\mu_q, \sigma_q^2) \end{aligned} \quad (3.2)$$

If we let

$$\begin{aligned} X &\approx N(\mu_q, \sigma_q^2) \\ U &\approx N(\mu_p - k\mu_x, \sigma_p^2 + k\sigma_q^2) \end{aligned} \quad (3.3)$$

one can see that the yield Y takes the form of $Z = \frac{X}{U}$, where X and U are independent normally distributed random variables. If X and U uphold the assumption for Independence and both of there means were zero, this would be a straightforward problem and the distribution would simply be that of a Cauchy. Since X and U do not both have mean zero, this problem is a bit more complicated. Leaving the derivation to the reader, the probability distribution for Z takes the form:

$$P_z(z, \mu_p, \mu_x, \delta_p, \delta_x) = Ae^{\frac{1}{2}((\frac{\mu_x}{\delta_x})^2 + (\frac{\mu_p}{\delta_p})^2)} + Be^C + Erf(D)$$

$$A = \frac{1}{\pi(z^2(\frac{\delta_p}{\delta_x}) + (1 + kz)^2(\frac{\delta_p}{\delta_x}))}$$

$$B = \frac{\frac{\delta_p}{\delta_x}(z\frac{\mu_x}{\delta_x}\frac{\delta_p}{\delta_x} + (1 + kz)\frac{\mu_p}{\delta_p})}{\sqrt{2\pi}(z^2(\frac{\delta_p}{\delta_x})^2 + (1 + kz)^2(\frac{\delta_p}{\delta_x}))^{\frac{3}{2}}}$$

(3.4)

$$C = \frac{(z\frac{\mu_p}{\delta_p}\frac{\delta_p}{\delta_x} - (1 + kz)\frac{\mu_x}{\delta_x})^2}{z(z^2(\frac{\delta_p}{\delta_x})^2 + (1 + kz)^2)}$$

$$D = \frac{z\frac{\mu_x}{\delta_x} + (1 + kz)\frac{\mu_p}{\delta_p}\frac{\delta_x}{\delta_p}}{\sqrt{2(z^2 + (1 + kz)^2(\frac{\delta_x}{\delta_p})^2)}}$$

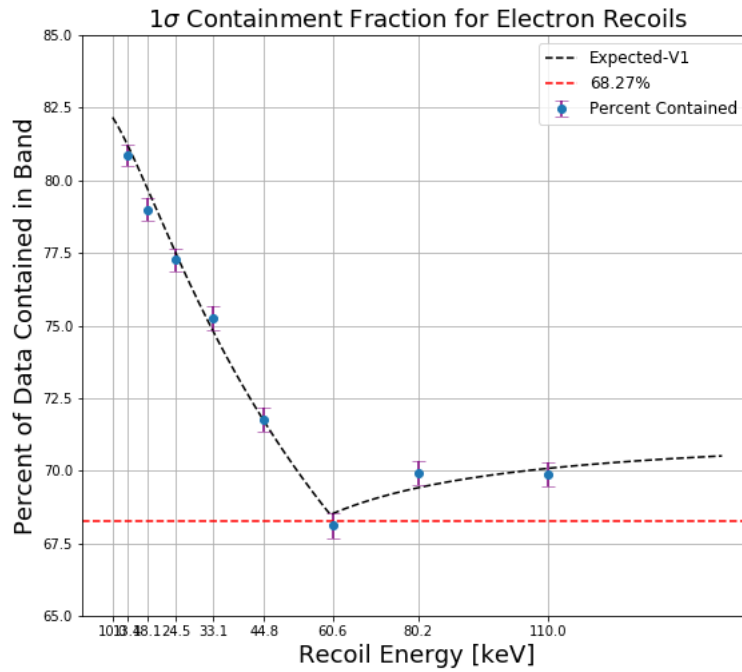
The probability distribution function for Z represents the pdf for the ratio distribution.

3.1.1 Model Validation

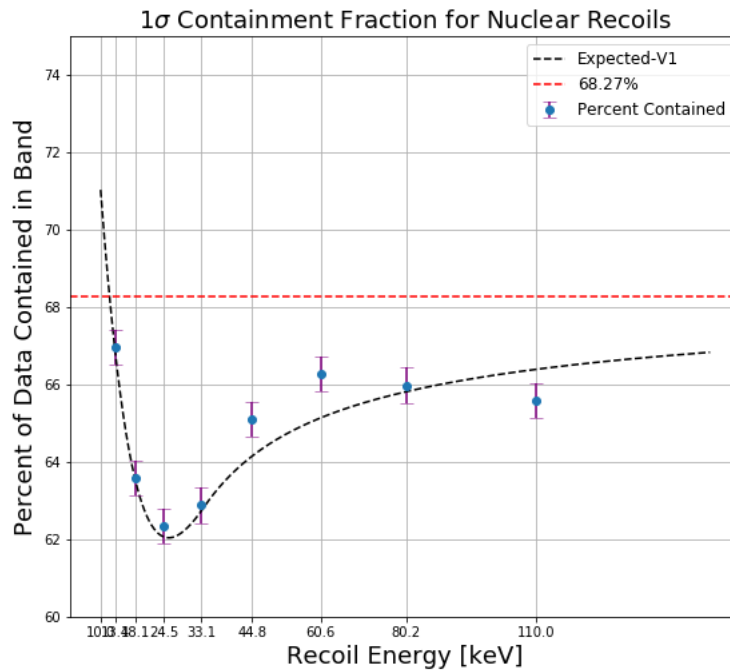
Now that there is a analytical expression for ionization yield for the electron and nuclear recoil band, we need to see if it matches with the simulated data. To do so, the containment fraction is calculated continuously from 10 - 130 keV by integrating equation 3.4 between the upper and lower 1σ bounds that are generated in equation 2.3.

$$\int_{-\sigma_Y}^{\sigma_Y} P_z(z, \mu_p, \mu_x, \delta_p, \delta_x) dz \quad (3.5)$$

The total area calculated between $-\sigma_Y$ and σ_Y determines how much data we should expecte to see within 1σ of the mean. Looking at Figure 3.1, we can see that the expected containment fraction matches what we see from the simulation for both.



(a)



(b)

Figure 3.1: ab) Containment fraction for electron recoils/ nuclear recoils generated with a fano factor included in the charge and phonon resolutions. Black dotted line represents expected containment fraction predicted by the PDF in equation 3.4.

3.2 Two Dependent Normal Distributions

In the previous section, a pdf for the ionization yield was derived. As shown, the expected containment fraction agreed with what was seen in the simulated data. The issues with the form of the pdf in the last section, is that the assumption that E_Q and E_P are not correlated is incorrect. In this section, a pdf for the yield assuming that E_Q and E_P are correlated will be derived. The containment fraction for the new pdf will then be compared with the containment fraction calculated from the simulated data in which the fano factor is included by varying the number of electron-hole pairs produced.

To make the derivation simpler, thinking about the yield as a function of 3 independent random variables makes for a slightly easier derivation for the probability distribution function:

$$Y = \frac{\epsilon N_{e/h} + X_Q}{E_r + X_P + \frac{V}{\epsilon} X_Q} \quad (3.6)$$

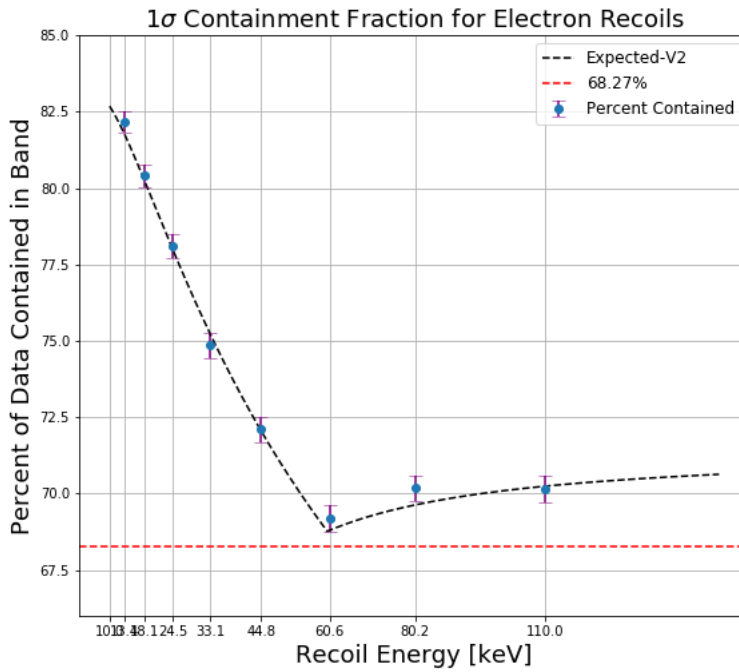
where E_r , V and ϵ are constants and N , X_Q and X_P are independent normally distributed random variables distributed as $N_{e/h} \approx N(\mu_N, \sigma_N^2)$, $X_Q \approx N(0, \sigma_Q^2)$, and $X_P \approx N(0, \sigma_P^2)$. Using a variable substitution, $A = \epsilon N + X_Q$ and $B = E_r + X_P + \frac{V}{\epsilon} X_Q$, then $Y = \frac{A}{B}$. We can then represent the pdf for the yield as:

$$F_{AB}(a, b) = \int_{-\infty}^{\infty} f_{ABX_Q}(a, b, q) dq \quad (3.7)$$

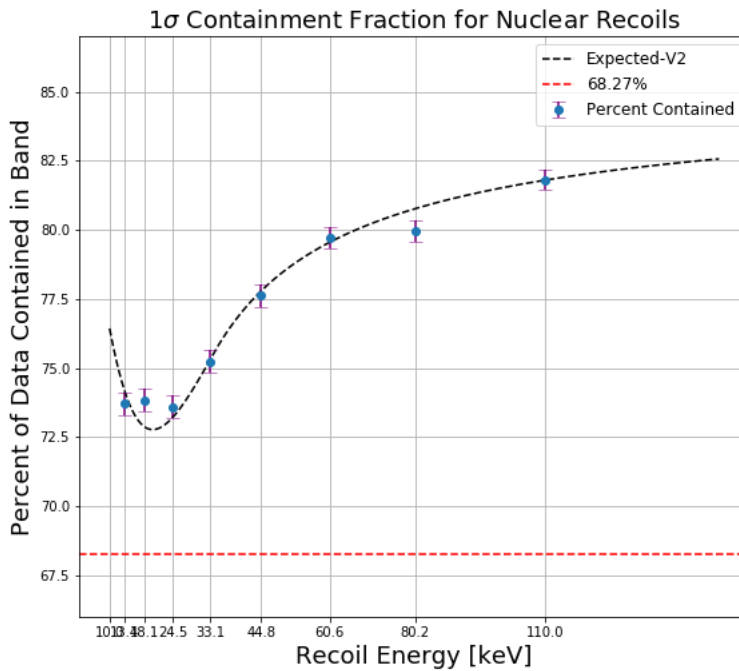
where $f_{ABX_Q}(a, b, q)$ is the joint distribution function. For a relatively detailed solution to deriving the pdf for dependent ratio distribution, please see appendix C.

The pdf for the yield is shown in equation 3.6. As with the independent version of the yield, the new pdf is used to compare the containment fraction for both the electron and nuclear recoil band. As shown in Figure 3.2, the expected containment fraction agrees with the data simulated by including the fano factor in the $N_{e/h}$ variation.

$$\begin{aligned}
 P(E_r, N_{e/h}, \delta_Q, \delta_P, \delta_N,) &= \frac{e^{-C}}{2A\pi\sqrt{k}} + \frac{Be^D}{2\sqrt{A}} \text{Erf}\left(\frac{B}{2\sqrt{A}}\right) \\
 A &= \frac{((x\frac{V}{\epsilon} + 1)\delta_Q)^2 + (x\delta_P)^2 + (\epsilon\delta_N)^2}{2k} \\
 B &= \frac{(\frac{V}{\epsilon}\delta_Q^2(E_r x \epsilon \bar{N}_{e/h}) + x \epsilon \bar{N}_{e/h}((\frac{V}{\epsilon}\delta_Q)^2) + \delta_P^2 + E_r(\delta_Q^2 + (\epsilon\delta_N)^2))}{k} \\
 C &= \frac{(((\bar{N}_{e/h}V + E_r)\delta_Q)^2 + ((\bar{N}_{e/h}\delta_P)^2 + (E_r\delta_N)^2)\epsilon^2)}{2k} \\
 D &= \frac{B^2}{4A} - C \\
 k &= \delta_P^2\delta_Q^2 + V^2\delta_Q^2\delta_N^2 + \epsilon^2\delta_N^2\delta_P^2
 \end{aligned} \tag{3.8}$$



(a)



(b)

Figure 3.2: ab) Containment fraction for electron recoils/ nuclear recoils generated with a fano factor included in the charge and phonon resolutions. Black dotted line represents expected containment fraction predicted by the PDF in equation 3.6.

CHAPTER IV

IMPACT ON DARK MATTER SEARCHES

As mentioned in chapter 1, as technology improves, dark matter communities are eliminating the parameter space in which dark matter is expected to be. With experiments such as CDMS looking for low mass WIMP dark matter, the effect of the Fano factor becomes increasingly important. As the Fano factor directly affects the width of the electron and nuclear recoil band. The higher the Fano factor, the wider the bands. If the Fano factor is moderately large, experiments lose the ability to discriminate between electron and nuclear recoils at low energies. In this section, the effect of the Fano factor on the lowest WIMP mass detectable will be investigated by looking at where 2σ containment bands overlap for electron and nuclear recoils as the Fano factor increases. The intersection of the two bands will dictate discrimination threshold, and thus, the lowest WIMP mass that can be detected.

This chapter will take a slightly different approach than the previous chapters. The last few chapters have been looking at the yield vs. recoil energy plane. Though the exact analytical distribution for the yield has been derived, the distribution can be pathological in some cases, and may not have a well defined standard deviation. For that reason, the following analysis will be carried out in the E_Q/E_P plane.

4.1 E_Q E_P Space

To look at the effect the Fano factor has on the minimum mass detectable, we need to first look at the data in the E_Q/E_P plane. Figure 4.1 shows the total charge energy vs phonon energy for electron recoils (pictured in black) and nuclear recoils (pictured in blue) simulated for recoil energies between 0 and 20 keV. One can see that there is clear separation between the bands until 10 keV in both E_Q and E_P . A property that makes E_Q/E_P space easier to analyze is the fact that for a fixed true recoil energy, the two dimensional distribution is a bivariate normal and therefore have a well defined standard deviation.

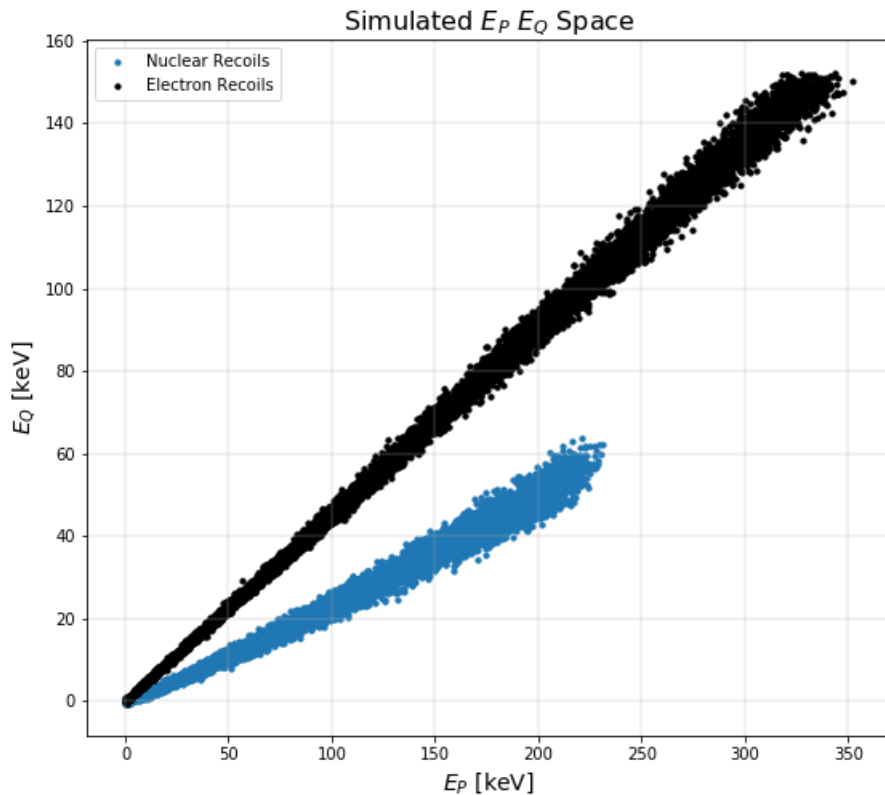


Figure 4.1: Simulated Charge energy (E_Q) - Phonon energy (E_P) plane for electron and nuclear recoils. Simulated for recoil energies ranging from 0 to 20 keV.

To begin the analysis, the E_Q/E_P bands are binned and simulated with a constant Fano factor ($F = 0.13$) for the electron recoil band and values from zero to one hundred in integer multiples of 10 for the nuclear recoil band. To see where the bands overlap, each bin is histogrammed and fit with a Gaussian in E_Q . The mean and standard deviation are calculated. For the electron recoil band, the lower 2σ bound is plotted for each bin and used to form a lower 2σ band for the entire energy range by fitting the data points to a line. The same procedure is used for the nuclear recoil band except an upper 2σ band is formed. Figure 4.2 and Figure 4.3 show the results of this procedure for 2 values of the Fano factor ($F=0$ and $F = 100$.) As expected, the location of the intersection point shifts to higher E_Q and E_P values.

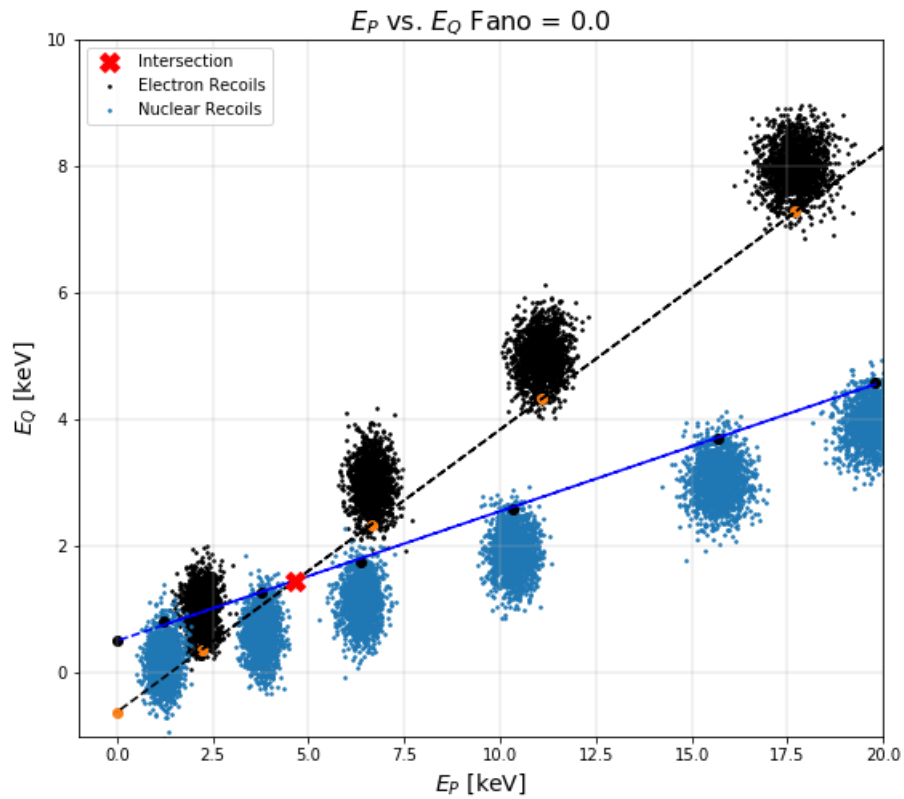


Figure 4.2: E_Q/E_P plan simulated with a Fano factor of 0. Black band represents electron recoils, blue band nuclear recoil bands. Orange and black points represent location of the 2σ mark for each bin. Data points are for to a line to form lower bound for electron recoils and upper bound for nuclear recoils. The red cross represents the intersection of the 2σ bands.

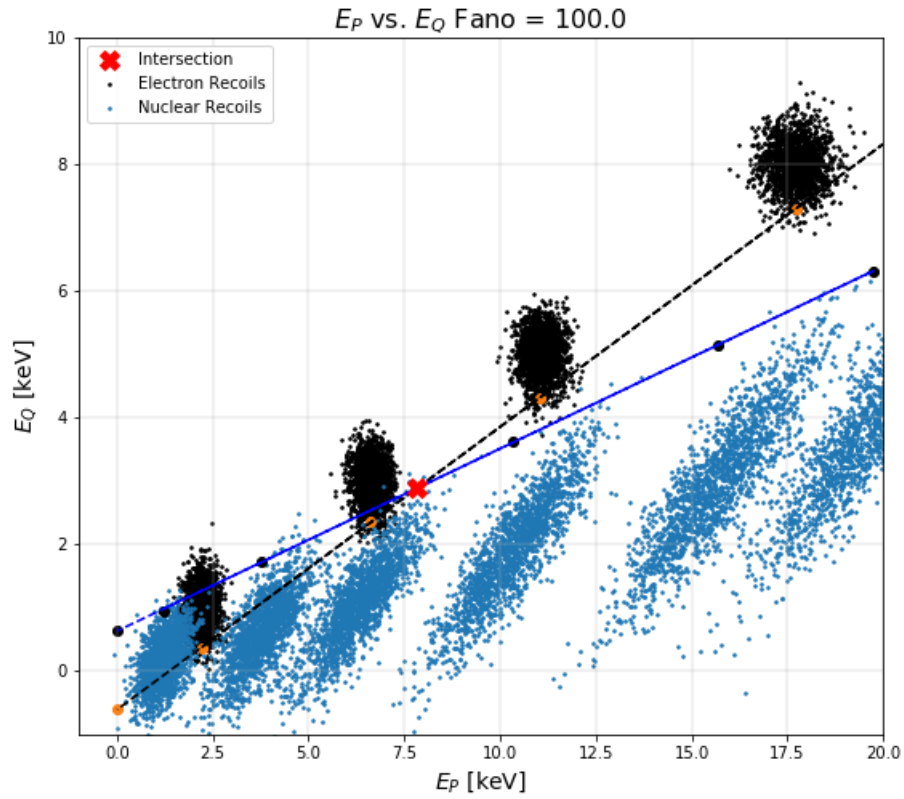


Figure 4.3: E_Q/E_P plan simulated with a Fano factor of 100. Black band represents electron recoils, blue band nuclear recoil bands. Red and black points represent location of the 2σ mark for each bin. Data points are for to a line to form lower bound for electron recoils and upper bound for nuclear recoils. The red cross represents the intersection of the 2σ bands

4.2 WIMP Mass Accessible

Direct detection dark matter experiments such as CDMS and Edelweiss are looking to move their parameter space to lower dark matter masses. If they are to be successful, experiments need to know the lowest energy in which they can distinguish between the electron and nuclear recoil band. In this section, the effect the Fano factor has on the smallest detectable dark matter mass will be investigated by using the intersection of the 2σ bands for electron and nuclear recoil bands in E_Q/E_P space.

To calculate the minimum mass detectable, one first needs to calculate the nuclear recoil energy of an event using the intersection point of the E_Q/E_P space plot:

$$E_{nr} = E_P - \frac{V}{\epsilon_\gamma} E_Q \quad (4.1)$$

Since we are interested in the minimum WIMP mass detectable, we assume that the nuclear recoil energy associated with the intersection point in Figure 4.3 represents the maximum amount of energy a WIMP can transfer to a germanium nucleus. When a WIMP deposits the maximum energy available, it scatters backward at 180° , which allows the use of 1D kinematics (conservation of energy and momentum) in the lab frame (earth frame):

$$\begin{aligned} KE_{\chi_i} &= KE_{\chi_f} + KE_{G_f} \\ P_{\chi_i} &= P_{\chi_f} + P_{G_f} \end{aligned} \quad (4.2)$$

where KE_{χ_i} and P_{χ_i} is the initial kinetic energy and momentum of the WIMP, KE_{G_f} and P_{G_f} is the kinetic energy and momentum of the Germanium nucleus after the collision. As we are assuming the germanium nucleus deposits all of its energy, the final kinetic energy of the germanium nucleus is equal to the nuclear recoil energy, $KE_{G_f} = E_{nr}$. Using this system of equations, we can solve for the WIMP mass as a function of nuclear recoil energy:

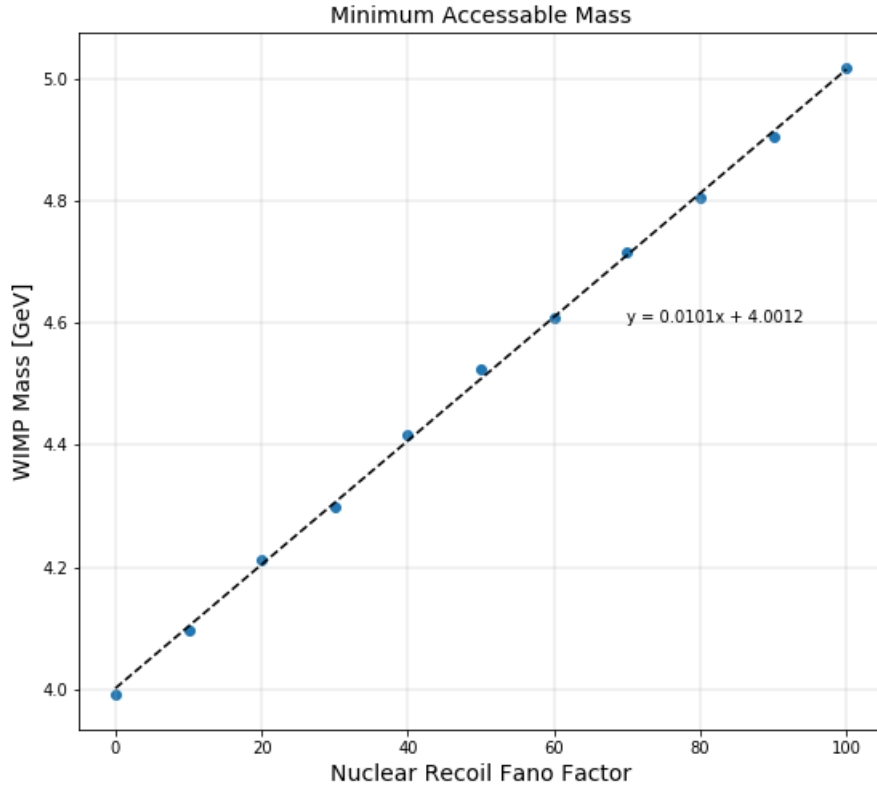


Figure 4.4: Minimum mass acceptable vs nuclear recoil Fano factor. Mass calculated using recoil energy corresponding to the intersection point in figures such as Figure 4.3.

$$M_\chi = \frac{M_G E_{nr}}{V_{max} \sqrt{2M_G E_{nr} - E_{nr}}} \quad (4.3)$$

where M_G is the mass of a Germanium nucleus, and V_{max} is approximately the maximum velocity a WIMP can have in the lab frame: $V_{max} = V_{escape} + V_{earth} + V_{solar}$. V_{max} is around 780 km/s [35].

Figure 4.4 shows the minimum mass detectable as a function of Fano factor. As expected, the minimum mass detectable increases with increasing Fano factor as we lose the ability to differentiate between electron and nuclear recoils at low energies with increasing Fano factor, motivating the need to measure this effect.

4.2.1 Effect on Dark Matter Limit

The Fano factor has the potential to effect where we can confidently remove parameter space for dark matter. For example, if we look at the silicon iZIP line in Figure 4.5, we can see a kink in the line where the cross section beings to steeply dive. This kink represents the transition between a background limited and a background free interval [23].

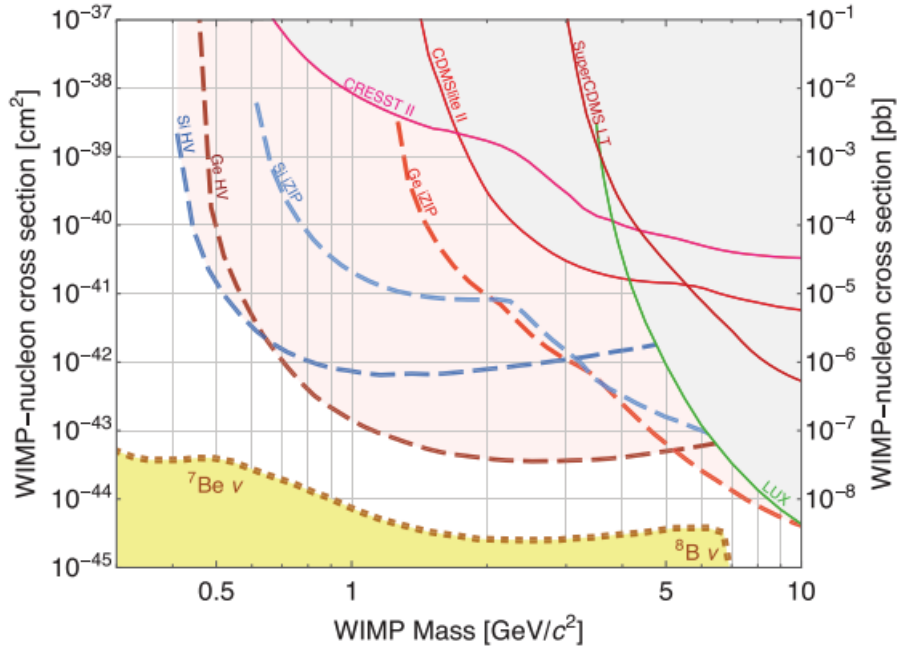


Figure 4.5: Projected exclusion sensitivity for the SuperCDMS SNOLAB direct detection dark matter experiment. The vertical axis is the spin-independent WIMP-nucleon cross section under standard halo assumptions, and the horizontal axis is the WIMP mass, where WIMP is used to mean any low-mass particle dark matter candidate. The blue dashed curves represent the expected sensitivities for the Si HV and iZIP detectors and the red dashed curves the expected sensitivities of the Ge HV and iZIP detectors [23]

In the background free situation the scientific impact can be improved by increasing the experiment's run time. However, the background limited situation cannot be improved without a detailed investigation into the background sources and engineering an overall cleaner experiment [36]. The minimum mass detectable may directly effect the location of this kink point. For example: if a measured value of a Fano factor was found to be 40, the minimum mass detectable would be 4.5 GeV. This would shift the kink point on the limit

curve to a higher WIMP mass, meaning the background limited situation would be applicable to more parameter space and therefore we would not be able to improve the limit simply by running longer for more of the WIMP mass parameter space.

APPENDIX A

SIMULATION ALGORITHM

1.1 Simulated Recoil Band Algorithm

The following algorithm is used to simulate the fraction of energy given to the electronic system, or yield, as a function of energy for electron and nuclear recoils.

1. Find the true recoil energy.
 - Create a uniform distribution of energy between 10 and 150 keV.
 - The true recoil energy is then randomly drawn for this distribution.
2. Calculate the average number of electron hole pairs produced \bar{N} based on the yield Y .
 - Y is the average yield calculated from Lindhard for a given recoil energy.
3. Randomly draw the number of electron hole pairs produced N
 - N is randomly drawn from a normal distribution with a mean of \bar{N} and a standard deviation $\sqrt{\bar{N}F}$, where F is the fano factor.
4. Calculate E_P and E_Q based on N .
 - E_P and E_Q are considered the "true" values.
5. Calculate detector resolutions σ_p and σ_q

- $\sigma_p(E_P)$ and $\sigma_q(E_Q)$ are based on the quantities found in Dan Jardin's note [ref].
6. Smear E_P and E_Q with σ_p and σ_q to find \tilde{E}_P and \tilde{E}_Q
 - Create two normal distributions with means E_P and E_Q and standard deviations σ_p and σ_q .
 - Randomly draw from these distributions to find \tilde{E}_P and \tilde{E}_Q respectively.
 7. Calculate the 'measured' recoil energy \tilde{E}_r using \tilde{E}_P and \tilde{E}_Q .
 8. Calculate the 'measured' yield \tilde{Y}

1.2 Expected Yield Algorithm

The following algorithm is to calculate the expected amount of energy given to the electronic system as a function of energy for electron and nuclear recoils.

1. Find the true recoil energy.
 - Create a uniform distribution of energy between 10 and 150 keV.
 - The true recoil energy is then randomly drawn for this distribution.
2. Calculate the average number of electron hole pairs produced \bar{N} based on the yield Y .
 - Y is the average yield calculated from Lindhard for a given recoil energy (for electron recoils $Y = 1$.)
3. Calculate \bar{E}_P and \bar{E}_Q based on \bar{N}
4. Calculate $\sigma_P(\bar{E}_P)$ and $\sigma_Q(\bar{E}_Q)$ based on Dan Jardin's note [ref]
5. Add $\epsilon^2 F \bar{N}$ to σ_Q^2 to get $\tilde{\sigma}_Q^2 = \sqrt{\sigma_Q(\bar{E}_Q)^2 + \epsilon^2 F \bar{N}}$
 - The fano factor F is added here, as we are not varying the number of electron hole pairs created.

6. Add $(eV)^2 F \bar{N}$ to $\tilde{\sigma}_P^2$

7. Find expected PDF for the yield using $\bar{E}_P, \bar{E}_Q, \tilde{\sigma}_P^2, \tilde{\sigma}_Q^2$.

APPENDIX B

DISTRIBUTION PLOTS

Shown below are the histograms and QQ plots for ionization yield for the electron and nuclear recoil bands. Data is generated using version 2 of the simulation (Varying number of electron-hole pairs.) Data was split into the following bins: [10,13.4,18.1,24.5,33.1,44.8,60.4,80.2,110]. Each plot is made made the the bin center.

2.1 Electron Recoils: Fano = 0.13

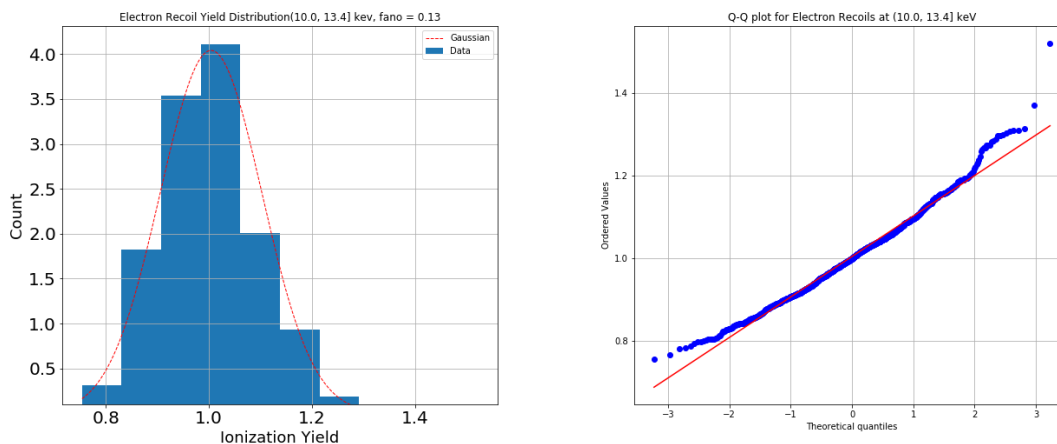
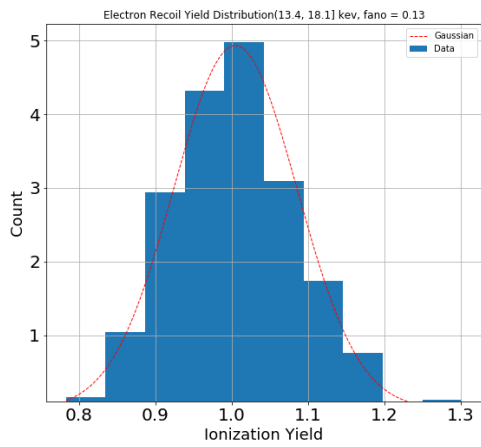
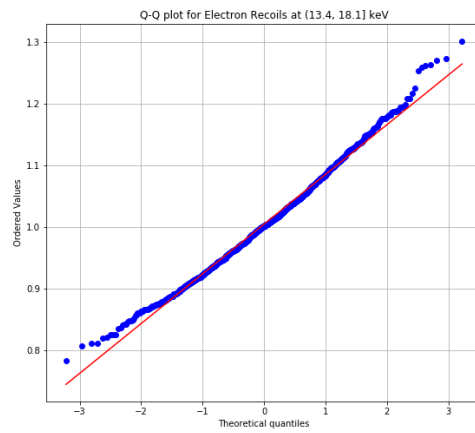


Figure 2.1: Histogram (a) and Q-Q plot (b) for electron recoils simulated at bin center 11.7 keV

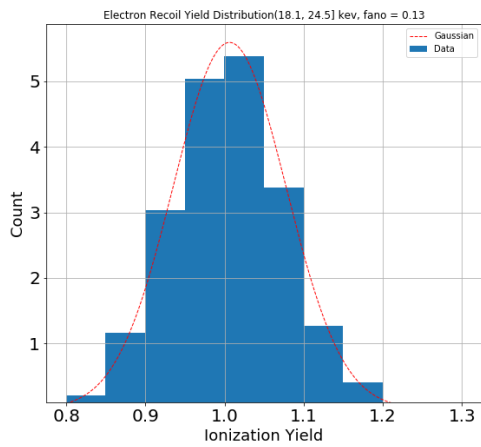


(a)

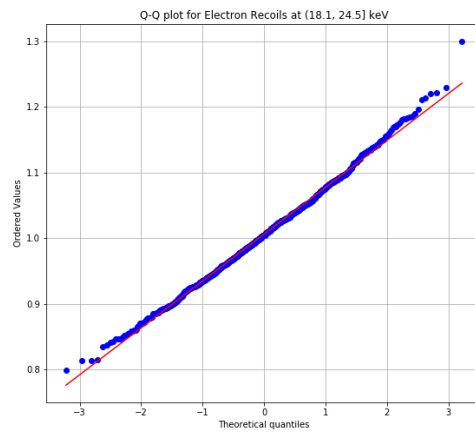


(b)

Figure 2.2: Histogram (a) and Q-Q plot (b) for electron recoils simulated at bin center 15.7 keV



(a)



(b)

Figure 2.3: Histogram (a) and Q-Q plot (b) for electron recoils simulated at bin center 21.3 keV

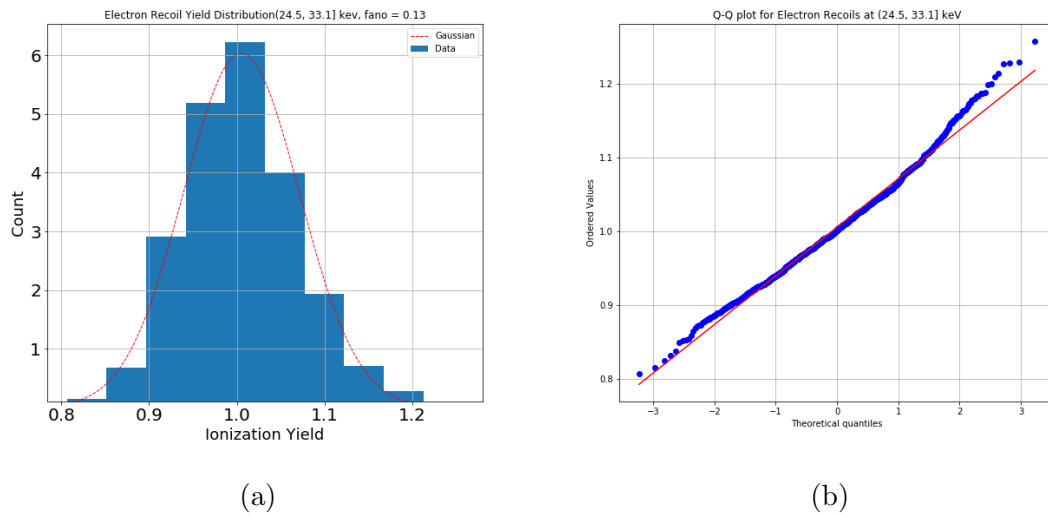


Figure 2.4: Histogram (a) and Q-Q plot (b) for electron recoils simulated at bin center 28.8 keV

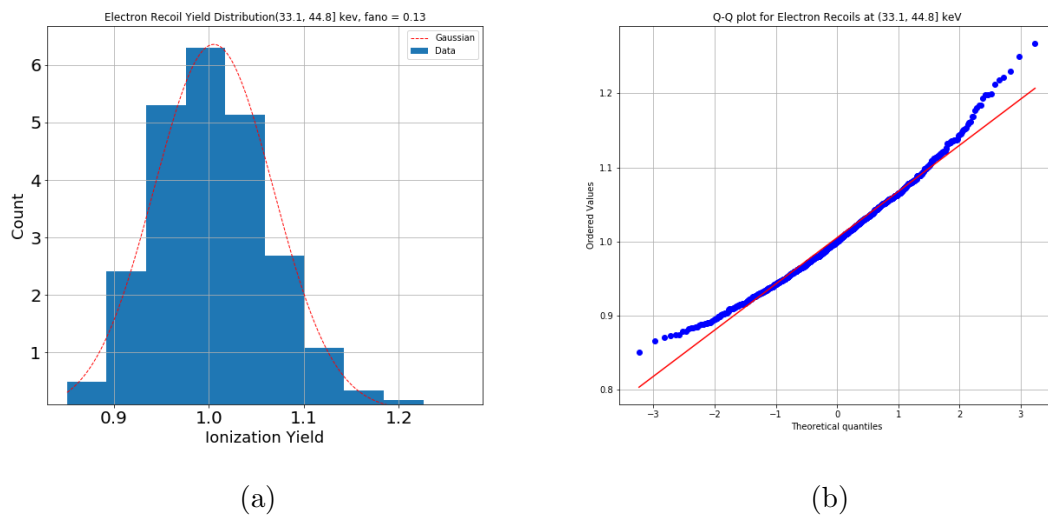
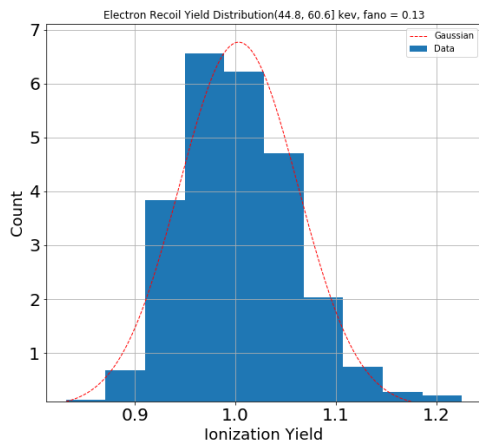
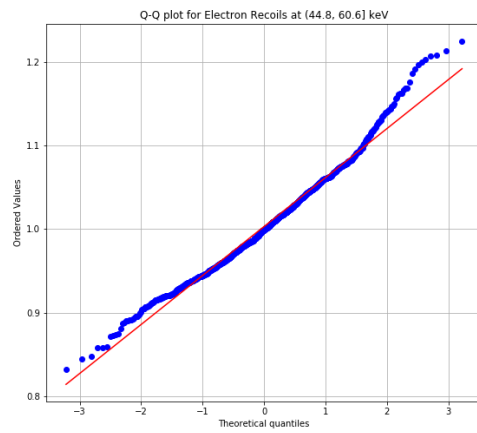


Figure 2.5: Histogram (a) and Q-Q plot (b) for electron recoils simulated at bin center 39.4 keV

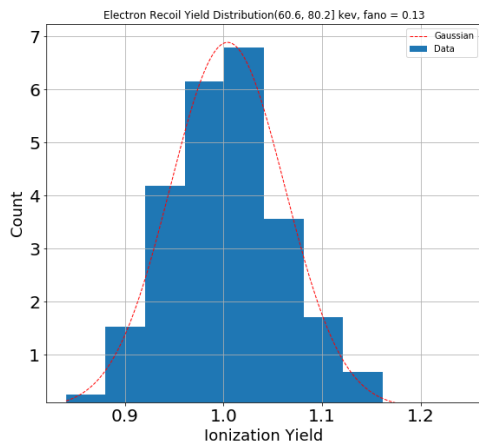


(a)

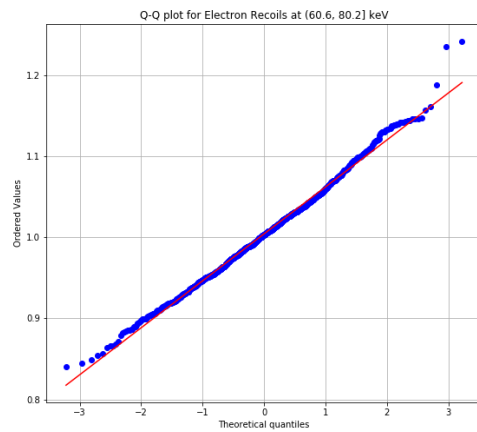


(b)

Figure 2.6: Histogram (a) and Q-Q plot (b) for electron recoils simulated at bin center 53.1 keV

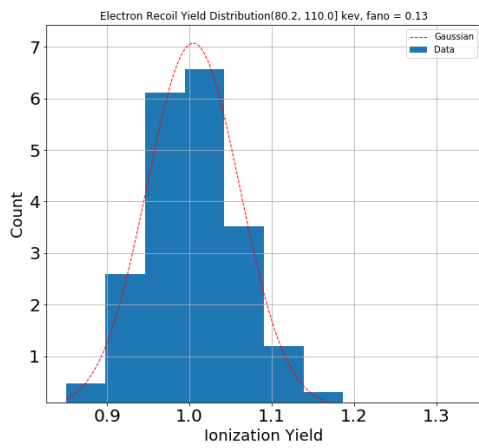


(a)

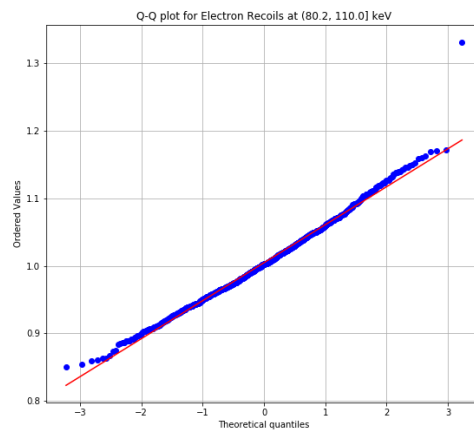


(b)

Figure 2.7: Histogram (a) and Q-Q plot (b) for electron recoils simulated at bin center 70.4 keV



(a)



(b)

Figure 2.8: Histogram (a) and Q-Q plot (b) for electron recoils simulated at bin center 95.1 keV

2.2 Nuclear Recoils: E_r Dependent Fano Factor

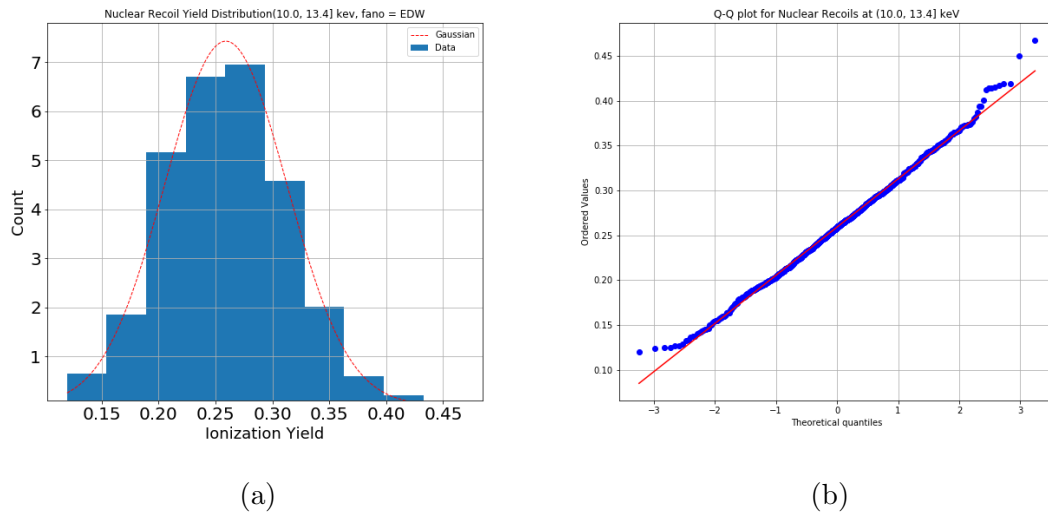
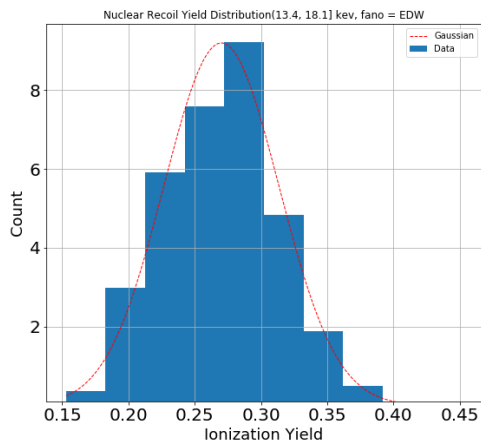
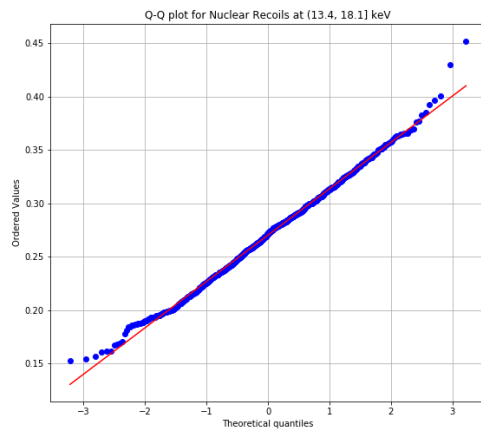


Figure 2.9: Histogram (a) and Q-Q plot (b) for nuclear recoils simulated at bin center 11.7 keV

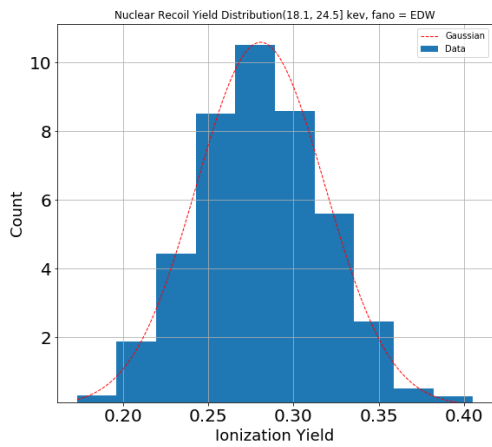


(a)

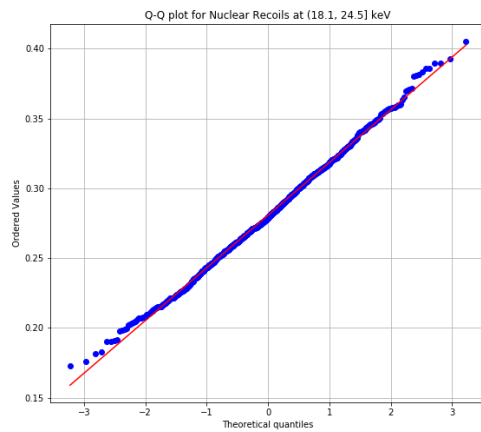


(b)

Figure 2.10: Histogram (a) and Q-Q plot (b) for nuclear recoils simulated at bin center 15.7 keV



(a)



(b)

Figure 2.11: Histogram (a) and Q-Q plot (b) for nuclear recoils simulated at bin center 21.3 keV

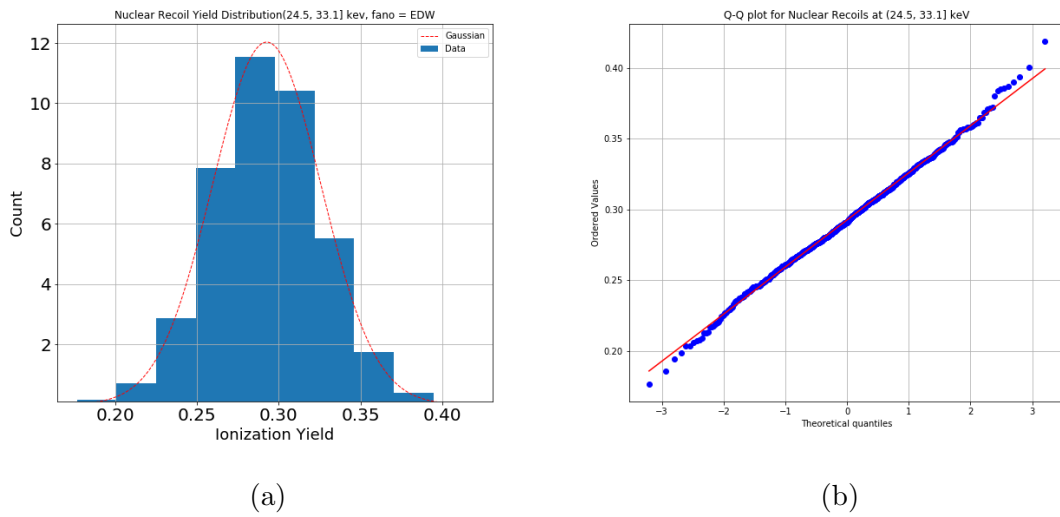


Figure 2.12: Histogram (a) and Q-Q plot (b) for nuclear recoils simulated at vbin center 28.8 keV

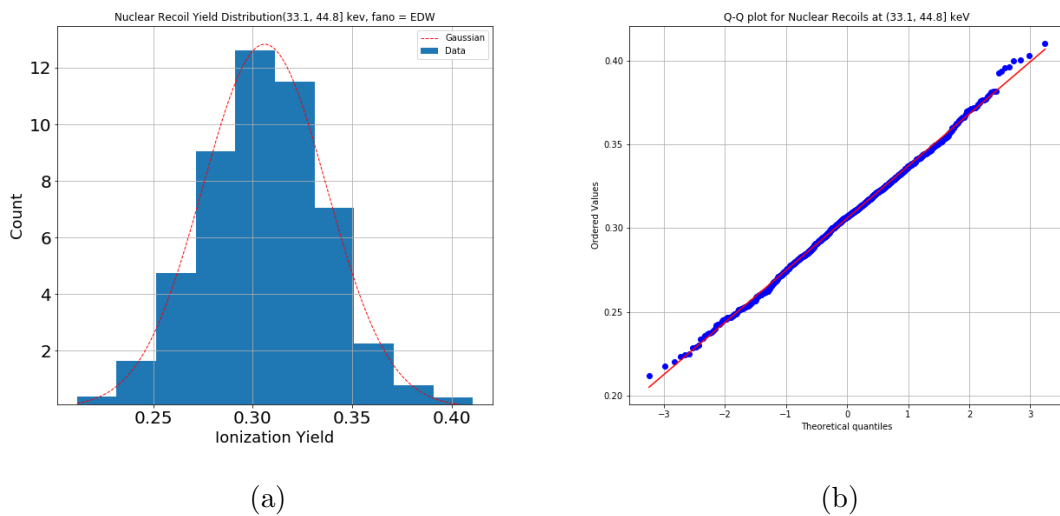
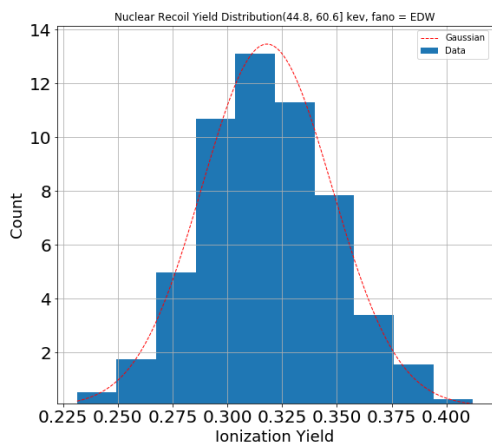
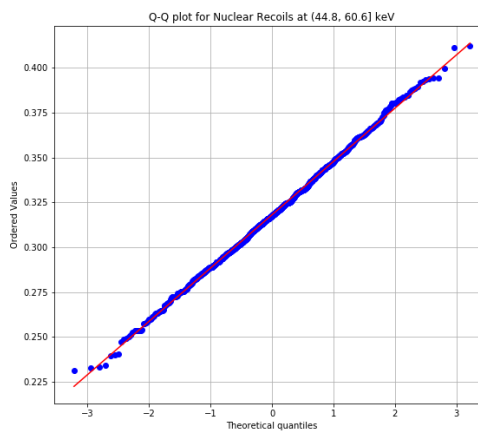


Figure 2.13: Histogram (a) and Q-Q plot (b) for nuclear recoils simulated at bin center 39.4 keV

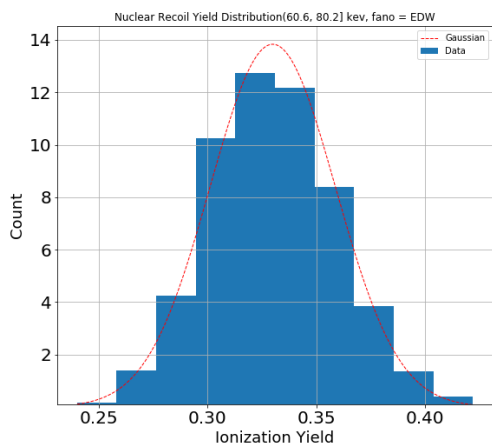


(a)

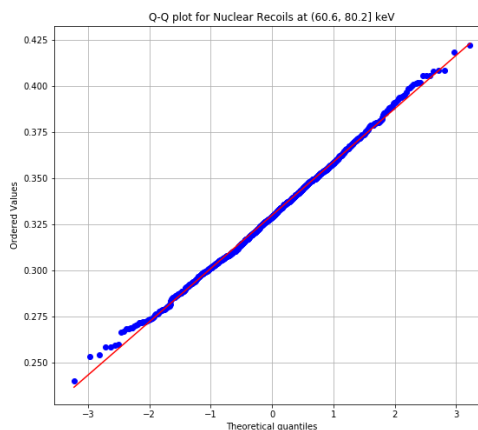


(b)

Figure 2.14: Histogram (a) and Q-Q plot (b) for nuclear recoils simulated at bin center 53.1 keV

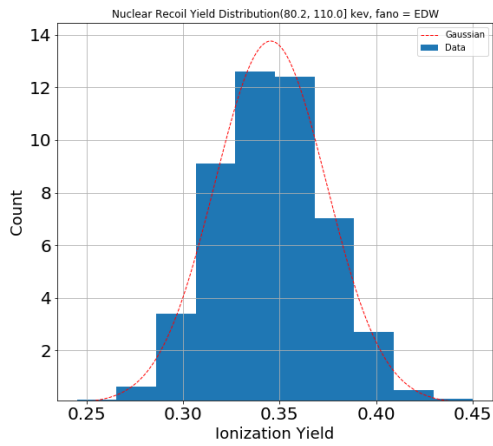


(a)

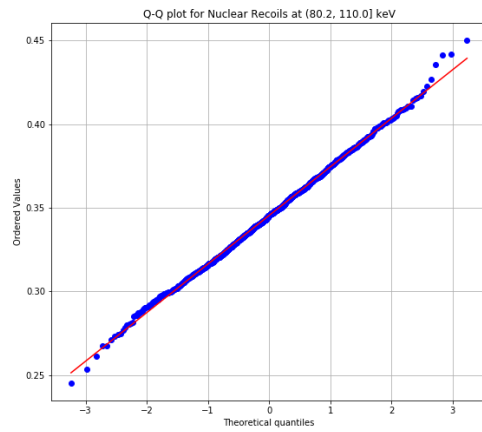


(b)

Figure 2.15: Histogram (a) and Q-Q plot (b) for nuclear recoils simulated at bin center 70.4 keV



(a)



(b)

Figure 2.16: Histogram (a) and Q-Q plot (b) for nuclear recoils simulated at bin center 95.1 keV

APPENDIX C

YIELD DISTRIBUTION

Prerequisite Information

Properties of Random Variables

- If X and Y are two continuous random variables described by probability density functions $f_X(x)$ and $f_Y(y)$ respectively, then the joint distribution is defined as follows.

$$f_{XY}(x, y) P\left(X = x \cap Y = y\right) = f_X(x|Y = y) f_Y(y) = f_X(x) f_Y(y|X = x) \quad (3.1)$$

- If X and Y are three continuous random variables described by probability density functions $f_X(x)$ and $f_Y(y)$ respectively, then the following property holds:

$$f_X(x) = \int_{y \in \Omega_Y} f_{XY}(x, y) dy \quad (3.2)$$

where Ω_Y is the set of all possible values of the variable Y . This leads to the next property:

- If X , Y , and Z are three continuous random variables described by probability density functions $f_X(x)$, $f_Y(y)$, and $f_Z(z)$ respectively, then the following property holds

$$f_{XY}(x, y) = \int_{z \in \Omega_Z} f_{XYZ}(x, y, z) dz \quad (3.3)$$

Ratio Distribution Density Function

- If X and Y are two continuous random variables described by probability density functions $f_X(x)$ and $f_Y(y)$ respectively, then the ratio distribution defined as $Z = \frac{X}{Y}$ has a density function that can be calculated through the following formula. (See Proof)

$$f_Z(z) = \int_{t \in \Omega_Y} |t| f_{XY}(zt, t) dt \quad (3.4)$$

Proof of Denisty Function for Yield Variable

In the current model of the Yield, the random variable is given by the following expression:

$$Y = \frac{\varepsilon N + X_Q}{E_r + X_P + \left(\frac{V}{\varepsilon}\right) X_Q} \quad (3.5)$$

where E_r , V , and ε are constants and N , X_Q , and X_P are independent normally distributed variables distributed as $N \sim N(\mu_N, \sigma_N^2)$, $X_Q \sim N(0, \sigma_Q^2)$, and $X_P \sim N(0, \sigma_P^2)$. Thus, the known density functions are $f_N(x) = \frac{1}{\sigma_N \sqrt{2\pi}} e^{-\frac{(x-\mu_N)^2}{2\sigma_N^2}}$, $f_{X_Q}(x) = \frac{1}{\sigma_Q \sqrt{2\pi}} e^{-\frac{x^2}{2\sigma_Q^2}}$, and $f_{X_P}(x) = \frac{1}{\sigma_P \sqrt{2\pi}} e^{-\frac{x^2}{2\sigma_P^2}}$.

A variable switch was introduced where $A = \varepsilon N + X_Q$ and $B = E_r + X_P + \left(\frac{V}{\varepsilon}\right) X_Q$.

Thus:

$$Y = \frac{\varepsilon N + X_Q}{E_r + X_P + \left(\frac{V}{\varepsilon}\right) X_Q} = \frac{A}{B} \quad (3.6)$$

Using the Ratio distribution density function formula gives the distribution of the Yield as:

$$f_Y(y) = \int_{-\infty}^{\infty} |t| f_{AB}(yt, t) dt \quad (3.7)$$

Now, the joint distribution $f_{AB}(a, b)$ must be calculated. Using the third listed property of random variables, we have:

$$f_{AB}(a, b) = \int_{-\infty}^{\infty} f_{ABX_Q}(a, b, q) dq \quad (3.8)$$

In order to calculate the joint distribution $f_{ABX_Q}(a, b, q)$, we use the first listed property of random variables, where:

$$f_{ABX_Q}(a, b, q) = f_{AB}(a, b | X_Q = q)_{X_Q}(q) \quad (3.9)$$

Then, because A and B are independent without X_Q , the conditional joint distribution can be calculated as:

$$f_{AB}(a, b | X_Q = q) = f_A(a | X_Q = q)_{X_Q} f_B(b | X_Q = q) \quad (3.10)$$

The remaining conditional variables are then:

$$\begin{aligned} A | (X_Q = q) &= \varepsilon N + q \sim N(\varepsilon \mu_N + q, \varepsilon^2 \sigma_N^2) \\ B | (X_Q = q) &= E_r + X_P + \left(\frac{V}{\varepsilon}\right) q \sim N\left(E_r + \left(\frac{V}{\varepsilon}\right) q, \sigma_P^2\right) \end{aligned} \quad (3.11)$$

Then, the probability density functions to plug in are:

$$\begin{aligned}
 f_{X_Q}(x) &= \frac{1}{\sigma_Q \sqrt{2\pi}} e^{-\frac{x^2}{2\sigma_Q^2}} \\
 f_A(x|X_Q = q) &= \frac{1}{\varepsilon \sigma_N \sqrt{2\pi}} e^{-\frac{(x - (\varepsilon \mu_N + q))^2}{2\varepsilon^2 \sigma_N^2}} \\
 f_B(x|X_Q = q) &= \frac{1}{\sigma_P \sqrt{2\pi}} e^{-\frac{(x - (E_T + (\frac{V}{\varepsilon})q))^2}{2\sigma_P^2}}
 \end{aligned} \tag{3.12}$$

Thus, summarizing previous steps:

$$\begin{aligned}
 f_Y(y) &= \int_{-\infty}^{\infty} |t| f_{AB}(yt, t) dt = \int_{-\infty}^{\infty} |t| \int_{-\infty}^{\infty} f_{ABX_Q}(yt, t, q) dq dt \\
 &= \int_{-\infty}^{\infty} |t| \int_{-\infty}^{\infty} f_{AB}(yt, t|X_Q = q)_{X_Q}(q) dq dt \\
 &= \int_{-\infty}^{\infty} |t| \int_{-\infty}^{\infty} f_A(yt|X_Q = q)_B(t|X_Q = q)_{X_Q}(q) \\
 &= \frac{1}{\varepsilon \sigma_P \sigma_Q \sigma_N (2\pi)^{\frac{3}{2}}} \int_{-\infty}^{\infty} |t| \int_{-\infty}^{\infty} e^{-\frac{1}{2} \left(\frac{q^2}{\sigma_Q^2} + \frac{(yt - (\varepsilon \mu_N + q))^2}{\varepsilon^2 \sigma_N^2} + \frac{(\varepsilon t - (\varepsilon E_T + Vq))^2}{\varepsilon^2 \sigma_P^2} \right)} dq dt
 \end{aligned} \tag{3.13}$$

Evaluating this expression gives the result of:

$$\begin{aligned}
P(E_r, N_{e/h}, \delta_Q, \delta_P, \delta_N) &= \frac{e^{-C}}{2A\pi\sqrt{k}} + \frac{Be^D}{2\sqrt{A}} \text{Erf}\left(\frac{B}{2\sqrt{A}}\right) \\
A &= \frac{((x\frac{V}{\epsilon} + 1)\delta_Q)^2 + (x\delta_P)^2 + (\epsilon\delta_N)^2}{2k} \\
B &= \frac{(\frac{V}{\epsilon}\delta_Q^2(E_r x \epsilon \bar{N}_{e/h}) + x \epsilon \bar{N}_{e/h}((\frac{V}{\epsilon}\delta_Q)^2) + \delta_P^2 + E_r(\delta_Q^2 + (\epsilon\delta_N)^2))}{k} \\
C &= \frac{(((\bar{N}_{e/h}V + E_r)\delta_Q)^2 + ((\bar{N}_{e/h}\delta_P)^2 + (E_r\delta_N)^2)\epsilon^2)}{2k} \\
D &= \frac{B^2}{4A} - C \\
k &= \delta_P^2\delta_Q^2 + V^2\delta_Q^2\delta_N^2 + \epsilon^2\delta_N^2\delta_P^2
\end{aligned} \tag{3.14}$$

Bibliography

- [1] van Albada T. S., Sancisi R., Petrou M., Tayler Roger John, Barrow John David, Peebles Phillip James Edwin, and Sciama Dennis William, “Dark matter in spiral galaxies,” vol. 320, no. 1556, pp. 447–464.
- [2] D. Clowe, M. Bradač, A. H. Gonzalez, M. Markevitch, S. W. Randall, C. Jones, and D. Zaritsky, “A direct empirical proof of the existence of dark matter*,” vol. 648, no. 2, p. L109.
- [3] N. A. Kurinsky, “The low-mass limit: Dark matter detectors with eV-scale energy resolution.”
- [4] P. Schneider, “Gravitational lensing statistics,” in *Gravitational Lenses* (R. Kayser, T. Schramm, and L. Nieser, eds.), vol. 406, pp. 196–208, Springer Berlin Heidelberg.
- [5] S. Weinberg, *Cosmology*. OUP Oxford. Google-Books-ID: rswTDAAAQBAJ.
- [6] A. Anderson, “The displacement of light rays passing near the sun,” vol. 104, no. 2614, p. 354.
- [7] L. Covi, J. E. Kim, and L. Roszkowski, “Axinos as cold dark matter,” vol. 82, no. 21, pp. 4180–4183.
- [8] P. Sikivie, “An argument that the dark matter is axions,”
- [9] K. van Bibber and G. Carosi, “Status of the ADMX and ADMX-HF experiments,”

- [10] S. J. Asztalos and Carosi, “SQUID-based microwave cavity search for dark-matter axions,” vol. 104, no. 4, p. 041301.
- [11] B. M. Brubaker and Zhong, “First results from a microwave cavity axion search at 24 micro-eV,” vol. 118, no. 6.
- [12] A. Boyarsky, O. Ruchayskiy, and M. Shaposhnikov, “The role of sterile neutrinos in cosmology and astrophysics,” vol. 59, no. 1, pp. 191–214.
- [13] K. N. Abazajian, M. Markevitch, S. M. Koushiappas, and R. C. Hickox, “Limits on the radiative decay of sterile neutrino dark matter from the unresolved cosmic and soft x-ray backgrounds,” vol. 75, no. 6, p. 063511.
- [14] H. Yüksel, J. F. Beacom, and C. R. Watson, “Strong upper limits on sterile neutrino warm dark matter,” vol. 101, no. 12, p. 121301.
- [15] L. Roszkowski, E. M. Sessolo, and S. Trojanowski, “WIMP dark matter candidates and searches—current status and future prospects,” vol. 81, no. 6, p. 066201.
- [16] P. Collaboration, “*Planck* 2015 results: XIII. cosmological parameters,” vol. 594, p. A13.
- [17] SuperCDMS Collaboration, “Low-mass dark matter search with CDMSlite,” vol. 97, no. 2.
- [18] P. N. Luke, “Voltage-assisted calorimetric ionization detector,” vol. 64, no. 12, pp. 6858–6860.
- [19] P. Sorensen, “Atomic limits in the search for galactic dark matter,” vol. 91, no. 8.
- [20] CDMS Collaboration, “Search for inelastic dark matter with the CDMS II experiment,” vol. 83, no. 11, p. 112002.

- [21] V. S. M. Lindhard, J. Nielsen, “Integral equations governing radiation effects. (notes on atomic collision, iii),” *Vidensk. Selsk 33*, vol. 10, 1963.
- [22] A. Kennedy, *SuperCDMS Prototype Detector Design and Testing*. PhD thesis, University of Minnesota, 2017.
- [23] R. Agnese, Anderson, and SuperCDMS Collaboration, “Projected sensitivity of the SuperCDMS SNOLAB experiment,” vol. 95, no. 8.
- [24] R. C. Alig, S. Bloom, and C. W. Struck, “Scattering by ionization and phonon emission in semiconductors,” vol. 22, no. 12, pp. 5565–5582.
- [25] O. Martineau, A. Benoit, L. Bergé, A. Broniatowski, L. Chabert, B. Chambon, M. Chapellier, G. Chardin, P. Charvin, M. De Jésus, P. Di Stefano, D. Drain, L. Dumoulin, J. Gascon, G. Gerbier, E. Gerlic, C. Goldbach, M. Goyot, M. Gros, J. P. Hadjout, S. Hervé, A. Juillard, A. de Lesquen, M. Loidl, J. Mallet, S. Marnieros, N. Mirabolfathi, L. Mosca, X. F. Navick, G. Nollez, P. Pari, C. Riccio, V. Sanglard, L. Schoeffel, M. Stern, and L. Vagneron, “Calibration of the EDELWEISS cryogenic heat-and-ionization germanium detectors for dark matter search,” vol. 530, no. 3, pp. 426–439.
- [26] B. L. Dougherty, “Measurements of ionization produced in silicon crystals by low-energy silicon atoms,” vol. 45, no. 3, pp. 2104–2107.
- [27] T. Yamaya, R. Asano, H. Endo, and K. Umeda, “Measurement of the fano factor for protons on silicon,” vol. 159, no. 1, pp. 181–187.
- [28] T. E. Collaboration, E. Armengaud, Q. Arnaud, C. Augier, A. Benoît, L. Bergé, J. Billard, J. Blümer, T. de Boissière, A. Broniatowski, P. Camus, A. Cazes, M. Chapellier, F. Charlieux, M. De Jésus, L. Dumoulin, K. Eitel, N. Foerster, J. Gascon, A. Giuliani, M. Gros, L. Hehn, G. Heuermann, Y. Jin, A. Juillard,

- C. K  f  lian, M. Kleifges, V. Kozlov, H. Kraus, V. A. Kudryavtsev, H. Le-Sueur, S. Marnieros, X.-F. Navick, C. Nones, E. Olivieri, P. Pari, B. Paul, M.-C. Piro, D. Poda, E. Queguiner, S. Rozov, V. Sanglard, B. Schmidt, S. Scorza, B. Siebenborn, D. Tcherniakhovski, L. Vagneron, M. Weber, and E. Yakushev, “Measurement of the cosmogenic activation of germanium detectors in EDELWEISS-III,”
- [29] D. Jardin, “Charge and phonon resolution,” *Internal Note*, 2016.
- [30] T. Burch, “Definition of the er bands and yield distributions for mean and gradient corrected data,” *Internal Note*, 2009.
- [31] A. et al., “Low-threshold analysis of cdms shallow-site data,” *PhysRevD*, 2010.
- [32] R. Calkins, “Nuclear and electron recoil band fits for the tynf-precoiltnf yield plane,” *Internal Note*, 2015.
- [33] D. P. Doane and L. E. Seward, “Measuring skewness: A forgotten statistic?,” vol. 19, no. 2, pp. null–null.
- [34] K. P. Balanda and H. L. Macgillivray, “Kurtosis: A critical review,” vol. 42, no. 2, pp. 111–119.
- [35] C. Collaboration., “CDMSlite: A search for low-mass WIMPs using voltage-assisted calorimetric ionization detection in the SuperCDMS experiment,” vol. 112, no. 4.
- [36] D. R. Barker, *SuperCDMS Background Models for Low-Mass Dark Matter Searches*. PhD thesis, University of Minnesota, 2018.